High-resolution two-photon transcranial imaging of brain using direct wavefront sensing — Source link ↗

Congping Chen, Zhongya Qin, Sicong He, Shaojun Liu ...+5 more authors

Institutions: Hong Kong University of Science and Technology, Huazhong University of Science and Technology

Related papers:

- Effects of the murine skull in optoacoustic brain microscopy.

- A large, switchable optical clearing skull window for cerebrovascular imaging.

- Widefield fluorescence localization microscopy for transcranial imaging of cortical perfusion with capillary resolution

- In Vivo Optical Imaging of Brain Function

- In Vivo Multiphoton Imaging of Mouse Brain

High-resolution two-photon transcranial imaging of brain using direct wavefront sensing

Congping Chen[1,2,3,8], Zhongya Qin[1,2,3,8], Sicong He[1,2,3], Shaojun Liu[6,7], Shun-Fat Lau[2,4,5], Wanjie Wu[1,2,3], Dan Zhu[6,7], Nancy Y. Ip[2,4,5] and Jianan Y. Qu[1,2,3,*]

[1]*Department of Electronic and Computer Engineering, The Hong Kong University of Science and Technology, Clear Water Bay, Kowloon, Hong Kong, P. R. China*

[2]*State Key Laboratory of Molecular Neuroscience, The Hong Kong University of Science and Technology, Clear Water Bay, Kowloon, Hong Kong, P. R. China*

[3]*Center of Systems Biology and Human Health, The Hong Kong University of Science and Technology, Clear Water Bay, Kowloon, Hong Kong, P. R. China*

[4] *Division of Life Science, The Hong Kong University of Science and Technology, Clear Water Bay, Kowloon, Hong Kong, P. R. China*

[5] *Molecular Neuroscience Center, The Hong Kong University of Science and Technology, Clear Water Bay, Kowloon, Hong Kong, P.R. China*

[6]*Britton Chance Center for Biomedical Photonics, Wuhan National Laboratory for Optoelectronics, Huazhong University of Science and Technology, Wuhan, China*

[7]*MoE Key Laboratory for Biomedical Photonics, Collaborative Innovation Center for Biomedical Engineering, School of Engineering Sciences, Huazhong University of Science and Technology, Wuhan, China*

[8]*These authors contributed equally to this work.*

Corresponding author: eequ@ust.hk (J.Y.Q.)

Abstract

Imaging of the brain in its native state at high resolution poses major challenges to visualization techniques. Two-photon microscopy integrated with the thinned-skull or optical clearing skull technique provides a minimally invasive tool for *in vivo* imaging of the cortex of mice without activating immune response and inducing brain injury. However, the imaging contrast and resolution are severely compromised by the optical heterogeneity of the skull, limiting the imaging depth to the superficial layer. Here, we develop adaptive optics two-photon microscopy for high-resolution transcranial imaging of layer 5 pyramidal neurons up to 700 µm below pia in living mice. In particular, an

33 optimized configuration of imaging system and new wavefront sensing algorithm are
34 proposed for accurate correction for the aberrations induced by the skull window and brain
35 tissue. We investigated microglia-plaque interaction in living brain of Alzheimer's disease
36 and demonstrated high-precision laser dendrotomy and single-spine ablation.

37

38 **Introduction**
39   Direct visualization and manipulation of neurons, glia and microvasculature in their
40 native environment is crucial to understand how the brain functions. With the growth of
41 fluorescent protein and transgenic technology, two-photon excited microscopy has
42 become an indispensable tool for *in vivo* brain imaging of small rodents over recent decades
43 because of its high spatial resolution and optical-sectioning capability(1, 2). However, the
44 biggest obstacle for direct imaging of the brain in living animal is the opaque skull because
45 it attenuates both the excitation and emission photons of two-photon microscopy severely,
46 yielding poor image quality even in the superficial brain region.
47 The primary methods of providing optical access to the mouse brain are the open-skull and
48 thinned-skull protocols(3, 4). The major limitation of open-skull approach is that skull
49 removal will inevitably trigger the glia-mediated inflammatory reaction and disturb the
50 neuronal physiology(5). Although an exceedingly thin skull could provide an imaging
51 resolution close to that with an open-skull window at the superficial layer, the probability
52 of mechanical disruption of cortex and activation of neuroinflammation is high and optical
53 access is restricted to a very small area(4). Furthermore, an overly thinned skull is not
54 suitable for chronic *in vivo* imaging because the newly grown skull must be constantly
55 removed to ensure the optical quality of cranial window(4). To minimize the risk of brain
56 trauma and inflammation, skull can be mechanically thinned to a certain thickness (~ 50
57 µm) to effectively reduce the scattering while holding its structural integrity to protect the
58 underlying brain(6). Alternatively, optical clearing technique can improve the skull
59 transparency by degrading the collagen fibers and removing the inorganic minerals with
60 chemical reagents(7–9). However, aberrations arising in optical heterogeneity in the
61 mechanically thinned or chemically cleared skull hamper transcranial brain imaging
62 performance in both resolution and depth.
63   Adaptive optics (AO), originally developed for astronomical telescopes, has been
64 introduced recently to improve two-photon microscopy by correcting system- or sample-
65 induced aberrations(10, 11). The wavefront aberrations can be determined by either
66 direct(12–16) or indirect(17–19) methods. The direct wavefront sensing approach employs
67 a Shack-Hartman wavefront sensor (SHWS) to measure the wavefront distortion of the
68 nonlinear fluorescence guide star. This method is fast, robust and photon-efficient,
69 enabling two-photon imaging of layer 5 neurons through an open-skull cranial window(14,
70 15), and its application to the thinned skull window is limited to ~ 500 µm below the
71 pia(15). In this work, we developed AO two-photon microscopy for high-resolution

72 cortical imaging through both thinned-skull and optical clearing skull windows (**Fig. S1**).
73 We built an ultra-sensitive SHWS incorporating a microlens array and an electron-
74 multiplying charge-coupled device (EMCCD) to measure the wavefront of a descanned
75 two-photon excited fluorescent (TPEF) guide star. The wavefront distortion was fed to a
76 deformable mirror (DM) to introduce a compensating distortion to the excitation light,
77 correcting the aberrations. We optimized the excitation numerical aperture (NA) of the
78 microscope system, which alleviated the scattering of the excitation laser and also extended
79 the depth of direct wavefront sensing. We advanced the wavefront sensing algorithm by
80 averaging the Shack-Hartman images from arbitrarily distributed near-infrared (NIR)
81 guide stars in a three-dimensional (3D) subvolume, allowing the reliable determination of
82 aberration beneath the skull window and brain tissue. Using this system, we first
83 characterized the optical properties of the skull windows and then achieved *in vivo* neuronal
84 imaging in mouse brains with much improved resolution and signal intensity up to ~700
85 µm below pia. We then investigated the interaction between microglia and plaque in a
86 mouse model of Alzheimer's disease (AD). Taking advantage of the tight focus provided
87 by AO correction, we demonstrated precise laser-mediated dendrotomy and single-spine
88 ablation of layer 5 pyramidal neurons, and studied the microglial dynamic response to this
89 neuronal microsurgery.
90
91
92 **Results**
93
94 **Optimization of the imaging system configuration and new wavefront sensing**
95 **algorithm** We first optimized the microscope system for transcranial deep brain imaging
96 using a reduced NA excitation and a high NA collection configuration. This approach
97 aimed to mitigate optical scattering and aberrations of the excitation laser from the skull
98 window and brain tissue while maintaining a high collection efficiency of fluorescence
99 signal for imaging. As shown in **Fig. 1a**, the excitation NA could be reduced by underfilling
100 the back aperture of a high NA objective. To evaluate the effectiveness of this approach,
101 we conducted *in vivo* imaging of YFP-labelled neurons (Thy1-YFP mice) through a
102 thinned-skull window of 50 µm thickness with gradually decreasing the excitation NA
103 from 1.05 to 0.7. Despite the decrease of effective NA in the underfilled configuration, we
104 did not observe obvious degradation of the imaging resolution even in the topmost cortical
105 layers (**Fig. S2**). This should be attributed to the high-NA rays being highly scattered by
106 the skull/brain tissue and contributing little to the focus. Under the same excitation power,
107 the fluorescence intensity was enhanced up to twofold when reducing the excitation NA
108 from 1.05 to 0.7 (**Fig. 1b-c**). However, with further reduction of excitation NA, the imaging
109 resolution decreased (> 0.6 µm) and was not sufficient to visualize the fine structures such
110 as dendritic spines. These results indicated that using an underfilled objective is beneficial

111 for deep-brain imaging through a skull window, in agreement with another study of the
112 open-skull preparation(20). More importantly, because it is only necessary to correct
113 aberrations in the excitation path for two-photon microscopy, the reduction of focal cone
114 angle can also alleviate the scattering of the guide star signal, improve the quality of the
115 Shack–Hartmann spot image and enabled wavefront measurement at deeper region (**Fig.**
116 **1d-e** and **Fig. S3**). The benefits are attributed to that SHWS favorably collects the
117 descanned TPEF guide star signals from the reduced focal cone angle of excitation beam
118 and effectively rejects scattered fluorescence from higher NA. To further extend the depth
119 of wavefront measurement, we investigated how a NIR guide star could improve direct
120 wavefront sensing through a thinned-skull window(15). We labelled the microvasculature
121 with Evans Blue by using retro-orbital injection into Thy1-YFP mice. Evans Blue can be
122 excited efficiently with a 920 nm laser and emits fluorescence at 680 nm. We compared
123 the guide star images in SHWS generated using both kinds of fluorophores at the same
124 location. As shown in **Fig. S4**, Evans Blue provides much better guide star images than
125 YFP at all imaging depths, because of the reduced scattering at the longer wavelength
126 fluorescence emission.
127
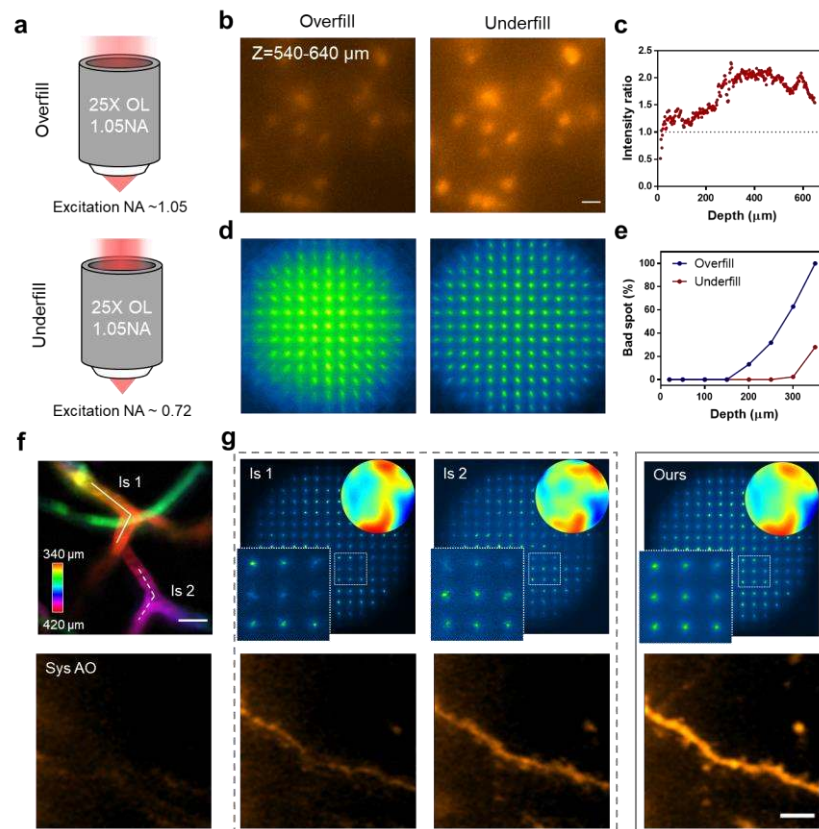
130 **Figure 1. Optimization of the excitation NA and new wavefront sensing algorithm for transcranial**
131 **brain imaging. (a)** Schematic illustration of a high-NA objective in the overfilled (top) and underfilled

132 (bottom) configuration. **(b)** xy maximum-intensity projection (MIP) images of the pyramidal neurons in
133 Thy1-YFP mice through a 50-µm thinned-skull window acquired using the overfilled (left) and underfilled
134 (right) objective. Imaging depth range: 540-640 µm. Scale bar: 20 µm. Details were presented in Fig. S2. **(c)**
135 Enhancement of signal intensity with depth by reducing the excitation NA. The intensity ratio is the average
136 intensity of the brightest 0.3% pixels in the xy image acquired with the underfilled objective divided by that
137 with the overfilled objective as shown in Fig. S2a. **(d)** Representative guide star images of YFP fluorescence
138 in Thy1-YFP mice when the objective was overfilled (left) and underfilled (right) at 250 µm below the
139 thinned skull. Details are shown in Fig. S3. **(e)** Percentages of bad spots in the Shack-Hartman spot image
140 for overfilled (blue) and underfilled (red) configuration. A bad spot is the one with poor signal quality to
141 make its center unidentifiable. **(f)** Top: Depth-coded images of the NIR-dye labeled microvascular vessels
142 for direct wavefront sensing. Two segments of vessels at different depths (solid line and dashed line labelled
143 with ls 1 and ls 2) were line scanned for wavefront measurement. Scale bar: 10 µm. Bottom: two-photon
144 images of YFP labelled dendrite with system correction only. **(g)** Top row: guide star images on the SHWS
145 with only ls 1 (left) or ls 2 (middle) and our algorithm (right). The left-bottom corners show magnified views
146 of the boxed regions and the right-top corners display the corrective wavefront pattern on the DM. Bottom
147 row: the corresponding AO corrected images. Details were presented in Fig. S7. Scale bar: 5 µm.

149 Since the skull is highly heterogeneous and contributes for the major aberrations, we
150 characterized the optical aberrations induced by the thinned-skull window in an *in vitro*
151 preparation. We created a 3D tissue phantom by dispersing fluorescent beads (0.2 µm in
152 diameter) in a mixture of Evans blue/agarose and then placing a piece of isolated thinned-
153 skull (50 µm in thickness) on top of the sample. Evans Blue fluorescence provided bright
154 and uniform guide stars for direct measurement of the aberrations of the thinned-skull
155 window, while the fluorescent beads were used to evaluate the PSF distortion caused by
156 the aberrations. Because the wavefront distortion varies spatially due to the skull
157 heterogeneity, we first investigated the isoplanatic FOV within which the aberrations were
158 similar. We performed AO corrections by averaging the aberrations over a series of FOV
159 ranges and compared the enhancement of the fluorescence intensity of the central bead
160 (**Fig. S5**). As can be seen, the aberrations would average out when the guide star was
161 scanned over a too large field, while if the scanned field is too small, tissue scattering yields
162 irregular Shack–Hartmann spots and induces errors in determining the aberration(13). The
163 optimal scanning FOV was found to be a square with sides of 30~60 µm (**Fig. S5b**).
164 Further, we characterized the aberrations of the thinned-skull window at various depths
165 (**Fig. S6**). The results showed that AO increased the fluorescence intensity up to 10-fold
166 and restored near-diffraction-limited resolution over 600 µm below the skull.
167 Next, we applied the AO approach to *in vivo* imaging of the mouse cortex in Thy1-YFP
168 mice. Evans blue was retro-orbitally injected to label the brain vasculature and served as
169 the guide star in the deep brain region. To measure the aberrations, we excited the labelled
170 microvessels in 60×60 µm^2 and integrated the de-scanned fluorescence signal on the
171 SHWS. However, because the brain tissue and the overlying skull were so heterogeneous,
172 the Shack–Hartmann spots became irregular and asymmetrical even when the guide star
173 signal was scanned over a segment of blood vessel (**Fig. 1f-g**). This induced large errors in

5

174 spot center identification and wavefront measurement, resulting in inaccurate or
175 incomplete AO correction. Given that an isoplanatic correction is valid within a small 3D
176 volume ($60\times60\times60$ μm^3), not merely in a 2D focal plane, we developed a wavefront
177 reconstruction algorithm by summing the SHWS images captured at different depths within
178 the isoplanatic volume and then spatially filtering each spot with its neighbors (see
179 method). This approach yields a clear image of Shack–Hartmann spots and single spots
180 stand out in each cell of the SHWS, enabling more accurate aberration determination (**Fig.**
181 **1g**). By using this algorithm, we corrected the aberrations reliably and improved the
182 imaging performance (**Fig. 1g** and **Fig. S7**).

183

184 **High-resolution cortical imaging through the thinned-skull window**

185   Taking the advantage of the optimized imaging system, NIR guide star and new
186 algorithm of wavefront sensing, we conducted *in vivo* transcranial imaging of cortex
187 through a thinned skull of ~ 50-µm thickness in Thy1-YFP mice. As can be seen, even with
188 system aberration corrected, the neuronal dendrites and somata were severely blurred by
189 aberrations caused by skull and brain tissue (**Fig. 2a-c**). With full AO correction, however,
190 pyramidal neurons spanning hundreds of microns in depth could be resolved clearly, along
191 with the surrounding microvessels. Quantitative comparisons show that AO not only
192 dramatically enhanced the fluorescence intensity, but also recovered the optimal imaging
193 resolution at depths as great as 680 µm below the pia (**Fig2. a-c** and **Fig. S8**). These results
194 lead to the conclusion that AO is essential and efficient for high-resolution and deep-brain
195 imaging through minimally invasive thinned-skull windows.

196   Microglia, the brain-resident phagocytes, play a critical role in brain homeostasis and
197 neurological diseases. The resting microglia with motile processes are highly sensitive to
198 subtle changes in brain parenchyma, and can become activated rapidly with substantial
199 changes in morphology and function upon brain damage or injury(21). Therefore,
200 minimally invasive imaging tools with the ability to resolve the fine processes are crucial
201 for the study of microglial physiology in the native environment. Taking advantage of our
202 approach, we conducted *in vivo* imaging of Cx3Cr1-GFP mice with microglia labeled with
203 green fluorescence protein (GFP). We first examined whether the thinned-skull (50-µm
204 thickness) preparation triggered the inflammatory response of microglia using time-lapse
205 imaging. Here, ramification and surveillance of the microglial processes were quantified
206 and monitored following the thinned-skull surgery to evaluate the potential surgical effect
207 on microglia activation(22). As indicated by the ramified morphology and surveying
208 behavior (**Fig. S9**), the microglia were not activated and the "thick" thinned skull window
209 effectively protected underlying brain tissue. By virtue of the fast AO correction, we
210 sequentially measured and corrected the aberrations in each subvolume and then stitched
211 them together to form a mosaic image of large FOV. As can be seen, after full AO

212   correction, the branching processes of microglia can be visualized clearly across the entire
213   FOV 400 µm below the pia (**Fig. 2d-e**).
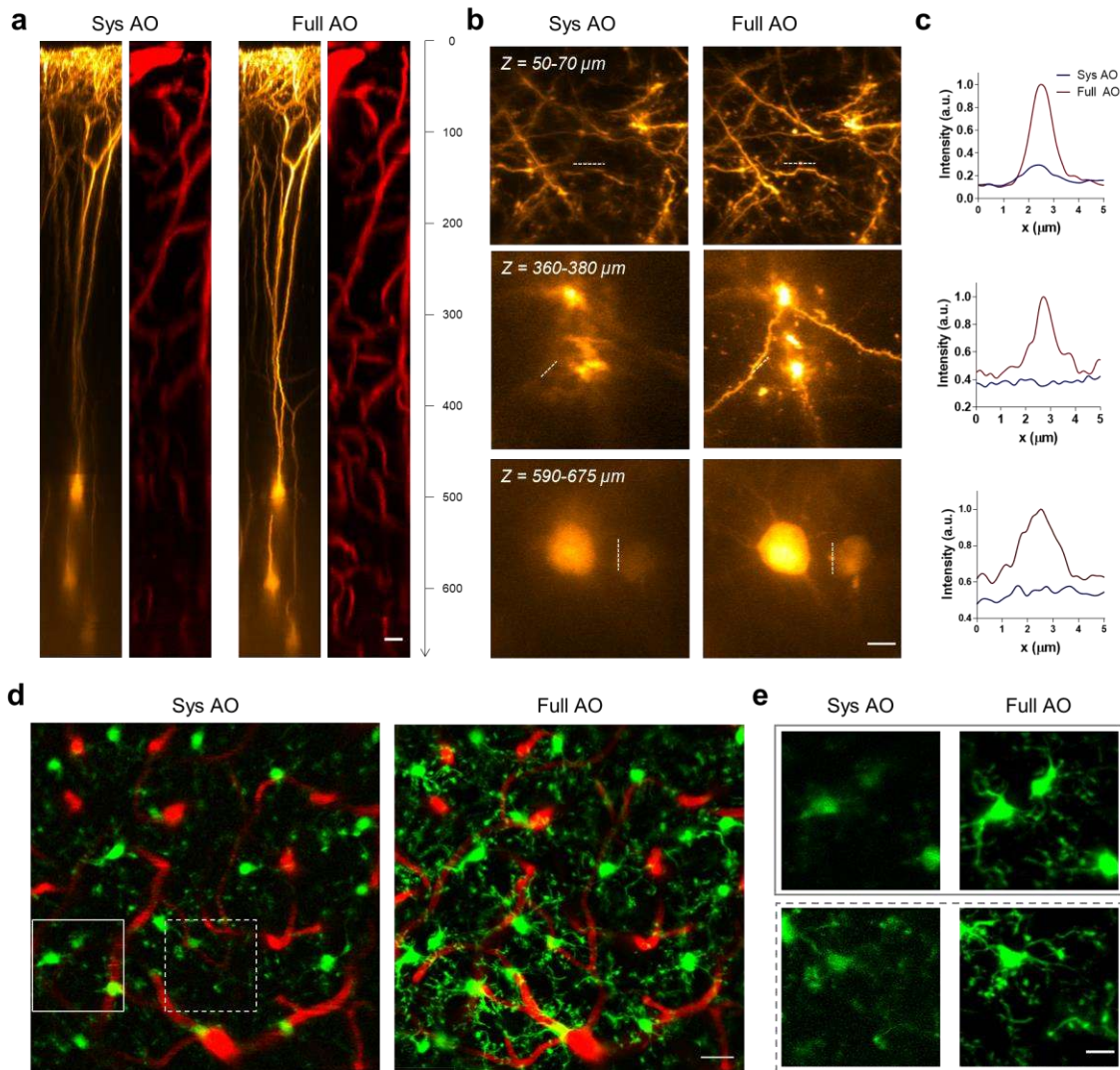
214
215
216   **Figure 2. *In vivo* AO imaging of the brain at high resolution through a thinned-skull window**. **(a)** xz
217   MIP images of the pyramidal neurons (orange) and microvasculature (red) in Thy1-YFP mice through a
218   thinned-skull window (50 µm in thickness) with system correction only (left) and full AO correction (right).
219   AO correction was performed every 50 µm of depth. Scale bar: 20 µm. **(b)** xy MIP of the stack images in (a).
220   Scale bar: 5 µm. **(c)** Intensity profiles along the dashed lines in (b) with system (blue) and full (red) AO
221   correction. **(d)** *In vivo* imaging of microglia (green) and microvessels (red) at 350-400 µm below the pia in
222   the Cx3Cr1-GFP mice with system (left) and full (right) AO corrections. Full AO correction were performed
223   every 40 µm and 5×5 subregions were stitched together to form the entire image. Scale bar: 20 µm. **(e)**
224   Magnified views of the boxed region in (d). Scale bar: 10 µm.
225

High-resolution cortical imaging through the optical clearing skull window

The optical clearing skull window is another technique for minimally invasive imaging of the brain(7–9). By degrading the collagens and inorganic minerals with chemical reagents, the scattering of the mouse skull can be reduced greatly, enabling *in vivo* imaging of the underlying cortex without disturbing brain homeostasis (**Fig. 3a** and **Fig. S10-11**). However, although the fluorescence intensity was enhanced tremendously after optical clearing, the imaging contrast and resolution were still low because of the skull-induced aberration (**Fig. 3a**). Following the study of AO imaging through thinned skull window, we sought to explore whether our AO approach could also improve imaging performance through optical clearing windows. The *in vitro* imaging results showed that despite the large aberration caused by the heterogeneity of skull and refractive index mismatch between the clearing reagents and water, our AO approach can recover the optimal imaging resolution effectively up to 500 µm below the skull (**Fig. S12**). *In vivo* imaging of the mouse cortex shows that AO improved the imaging resolution and fluorescence brightness up to 600 µm below the pia (**Fig. 3b-c**). Further, the branching processes of microglia can also be visualized clearly with AO correction (**Fig. 3d-e**), which allows us to study the dynamics of microglial processes in both physiological and pathological conditions. It should be noted that the imaging depth of the optical clearing skull window is smaller than the thinned skull preparation, likely due to the larger skull-induced scattering.
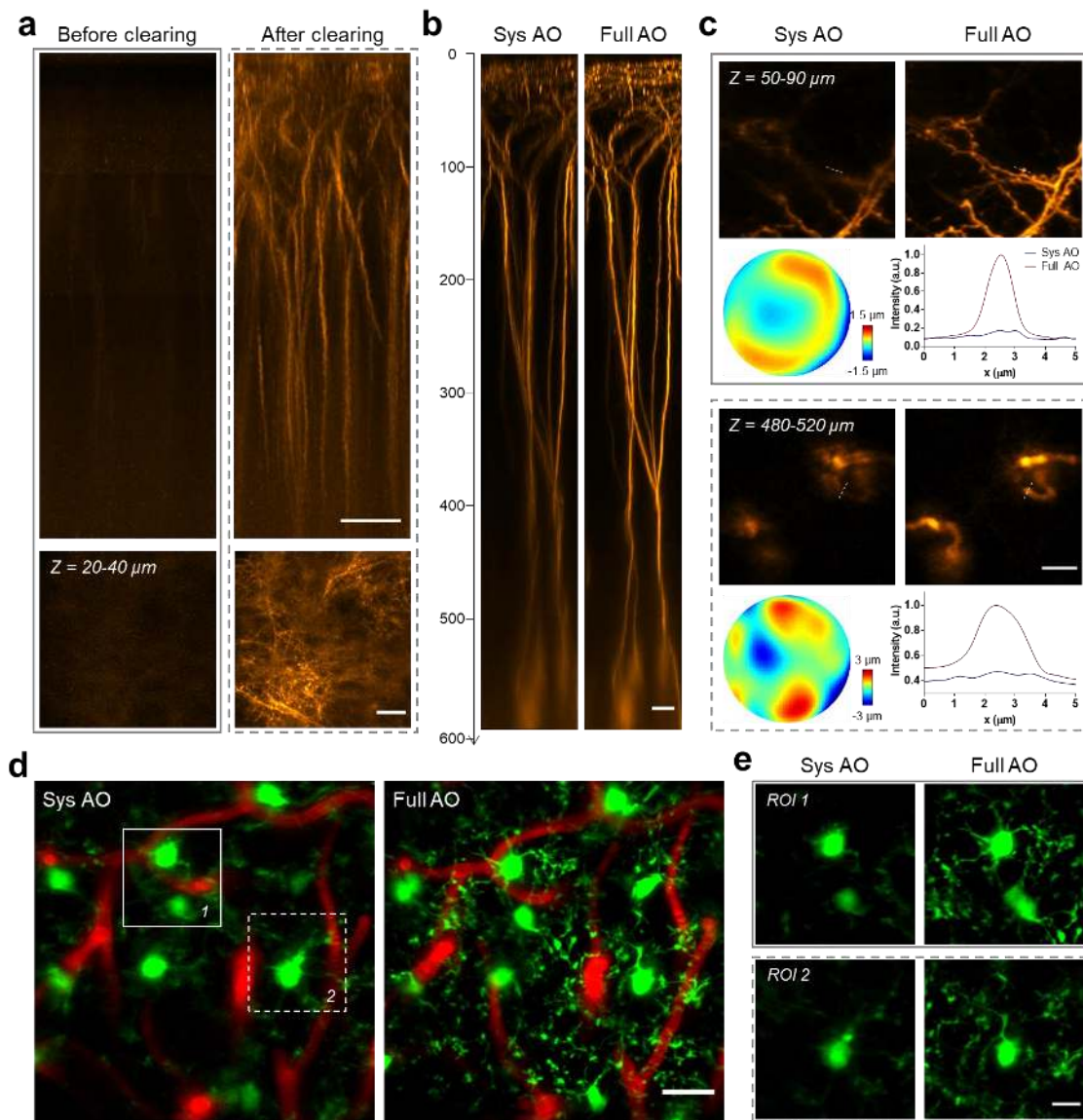
Figure 3. AO recovers high-resolution imaging of the cortex through an optical clearing window. **(a)** xz MIP of two-photon images of the YFP labelled neurons in the Thy1-YFP mice before (left) and after (right) optical clearing. Scale bar: 50 µm. Bottom row shows the xy MIP of the stack images. Scale bar: 20 µm. **(b)** xz MIP images of the pyramidal neurons in Thy1-YFP mice through the optical clearing window with system (left) and full (right) AO correction. AO correction was performed at every 50 µm depth. Scale bar: 20 µm. **(c)** xy MIP of the stack images in (b) at two representative depths and the corresponding corrective wavefront and intensity profiles along the dashed lines. Scale bar: 10 µm. **(d)** *In vivo* imaging of microglia (green) and microvessels (red) at 175-225 µm below the pia in the Cx3Cr1-GFP mice with system (left) and full (right) AO corrections. Full AO correction were performed every 40 µm and 3×3 subregions were stitched together to form the entire image. Scale bar: 20 µm. **(e)** Magnified views of images of the boxed regions in (d). Scale bar: 10 µm.

High-resolution imaging of microglia-plaque interaction and high-precision laser surgery

By using our AO two-photon microscope, we can perform high-resolution transcranial imaging in deep cortical layers without interrupting the brain homeostasis, which is crucial for the study of microglial roles with laminar characteristics under certain pathological conditions. For example, we investigated the microglial activity in the AD mice brain which has a laminar distribution of amyloid plaques(23). We observed significant morphological and functional differences between the plaque-associated and plaque-distant microglia in layer II/III of mice cortex (**Fig. 4a-b**). While the plaque-distant microglia has highly ramified processes with similar motility as that in the normal brain, the microglia surrounding the amyloid plaques shows less ramified morphologies with no obvious dynamics (**Fig. 4b**). These results indicate that normal microglia may undergo phenotype alteration that is associated with the layer-specific distribution of amyloid plaque during the progression of AD pathology. Our AO-assisted minimally invasive imaging method can also facilitate the therapeutic study on the microglia-mediated inflammation in AD.

Laser microsurgery, because of its high spatial precision of injury, has become a valuable tool for studying the cellular mechanisms that underlie various pathological phenomena such as neuronal degeneration and vascular disruption(24–27). However, high-precision laser surgery through skull windows is challenging because of large distortion of laser focus. We then applied the AO approach to study microglia-neuron interactions following laser-mediated neuronal injury through a thinned-skull window in Cx3Cr1-GFP/Thy1-YFP mice. We specifically targeted the first bifurcation point of the primary apical dendrite of a layer 5 pyramidal neuron and its neighboring compartments (**Fig. 4c**). As shown in **Fig. 4d-e,** the microglial processes and neuronal dendrites/ spines were clearly visualized using full AO correction. More importantly, AO also enabled precise laser microsurgery through the thinned-skull window, allowing us to ablate the branch point without influencing the nearby neurites, which is impossible otherwise. Time-lapse imaging revealed that the activation of microglia was highly correlated with the degeneration of the injured neuron (**Fig. 4f-g** and **Fig. S13**). While the local microglia near the injured site extended their processes rapidly towards the ablation point and completely wrapped around it within 10 minutes, microglia further away (either upper or deeper) also showed coordinated responses to the neuronal degeneration as indicated by decreased process motility (**Fig. 4f-g, Fig. S13** and **Movie. S1**). In addition, we also performed laser dendrotomy on a tuft dendrite of the layer 5 pyramidal neuron and high-precision single spine ablation without damaging the dendritic shaft and nearby spines, which resulted in distinct microglial responses (**Fig. S14** and **Movie. S2**). Although there is a chance that nearby unlabeled brain structures were injured, the removal of a single spine without influencing the parent dendrite indicates the submicron precision of AO-assisted laser

10

297   microsurgery. These results demonstrated the great potential of AO for precise optical
298   manipulation, in addition to high-resolution imaging.
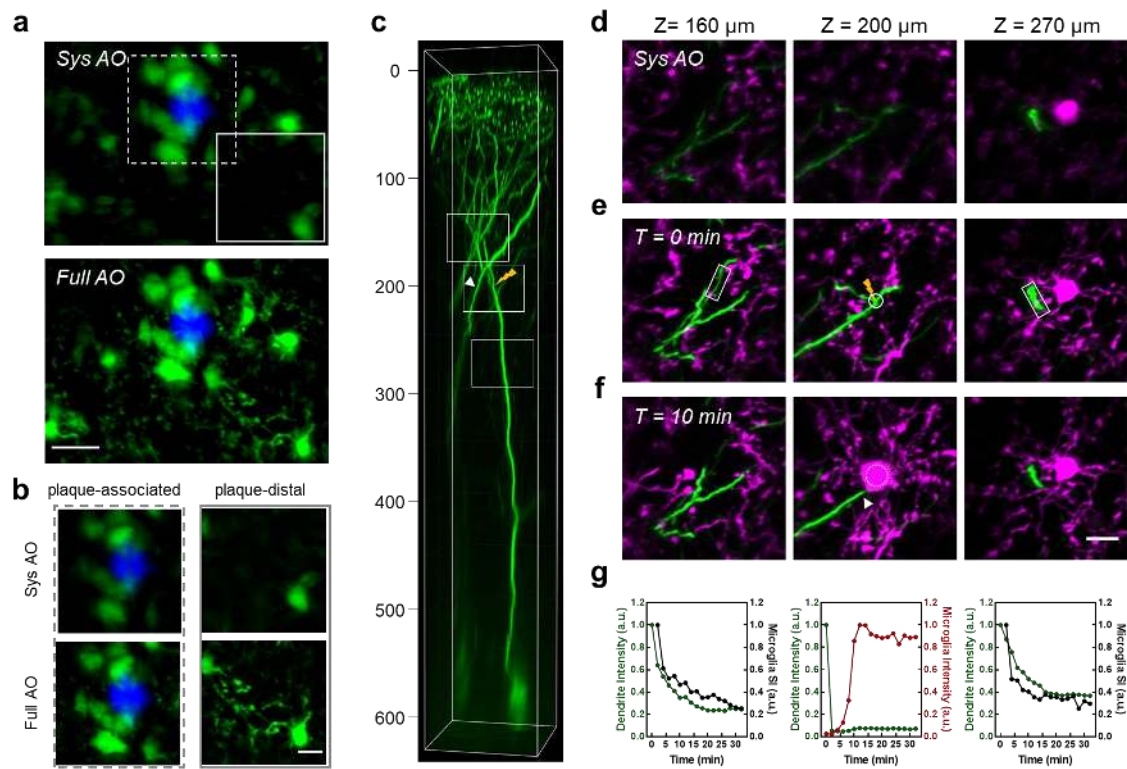
299

300   **Figure 4. Study of microglial activities in AD mice and neuron-microglial interactions following precise**
301   **laser micro-lesion**. **(a)** *In vivo* imaging of amyloid plaque(blue) and microglia (green) at 230-270 µm below
302   the pia in the APP-PS1/Cx3Cr1-GFP mice through a thinned-skull window with system (top) and full
303   (bottom) AO corrections. Full AO correction was performed every 40 µm and 3×3 subregions were stitched
304   together to form the entire image. Amyloid plaque was labeled by MeO-X04 through intraperitoneal
305   injection. Scale bar: 20 µm. **(b)** Magnified views of the boxed region in (a) showing the plaque-associated
306   (left) and plaque-distal (right) microglia. Scale bar: 10 µm. **(c)** 3D reconstruction of pyramidal neurons in
307   Thy1-YFP/Cx3Cr1-GFP mice through a thinned-skull window with full AO correction. **(d-e)** xy MIP images
308   of neuronal dendrites (green) and microglia (magenta) of the boxed region in (c) with system (d) and full (e)
309   AO correction before laser ablation. Imaging depths: left column, Z = 140-180 µm; middle column, Z = 180-
310   220 µm; right column, Z = 250-290 µm. The bifurcation point of the apical dendrite (Z = 200 µm) was
311   targeted for laser microsurgery (thunder symbol in (c) and middle panel of (e)). **(f)** Full AO corrected images
312   taken 10 minutes after laser ablation. The persistence of a nearby dendrite (arrowhead in (c) and the middle
313   plane of (f)) indicates the confinement of the laser injury. Scale bar: 10 µm. **(g)** Characterization of microglial
314   response to the dendritic degeneration. Left and right: microglial surveillance index (black line) and
315   fluorescence decay (green line) of the distal and proximal dendrites (boxed region in the left and right panel
316   of (e)); middle: influx of microglial processes to the injured spots represented by the microglial fluorescence
317   intensity (dotted circle in the middle panel of (f)) and the fluorescence decay of the injured dendrite (solid
318   circle in the middle panel of (e)).

319

Discussion

320
321   In this work, we advanced the imaging system and AO technique for high-resolution
322 deep-brain imaging through minimally invasive skull windows by employing a NIR guide
323 star within the microvasculature. In particular, we optimized the excitation NA of our
324 microscope system and showed that the use of an underfilled objective can not only
325 improve the excitation efficiency, but also benefits direct wavefront sensing of TPEF guide
326 stars. By scanning the NIR guide star within the microvasculature over a 3D subvolume
327 and subsequently employing a wavefront processing algorithm, we achieved *in vivo*
328 morphological imaging of layer 5 pyramidal neurons up to 700 µm below the 50-µm-
329 thickness skull. Further, by taking advantage of the optimal point spread function provided
330 by AO correction, we performed precise laser ablation of a single dendrite or spine and
331 studied the interaction between neurites and microglial cells following neuronal
332 microsurgery. Our results demonstrate that AO promises to advance the minimally invasive
333 imaging tools and facilitate neuroscience research in the living brain.

334   Because of the extreme optical inhomogeneity of skull bone, the aberration varies
335 quickly at different focal positions and the optimal corrective FOV is 30~60 µm for the
336 thinned-skull and optical clearing skull windows, which is smaller than that of the open-
337 skull cranial window (100 ~ 150 µm(14, 15, 28)). Thanks to fast AO correction by direct
338 wavefront sensing, we measured the aberrations sequentially for each subvolume and
339 stitched these subimages together to form an image of an entire large FOV. We have
340 demonstrated that by using a NIR guide star with an emission peak at ~ 680 nm, direct
341 wavefront sensing enabled imaging up to 700 µm below the pia through a thinned skull
342 window. The imaging resolution and contrast in deeper brain region are still compromised
343 by the dominant scattering caused by the skull and brain tissue. In this case, longer
344 excitation/emission wavelengths and even three-photon absorption process are
345 prefered(29, 30). In conjunction with emerging NIR fluorescent agents such as quantum
346 dots and organic conjugated polymer dots(31, 32), we expect that direct-wavefront-sensing
347 based AO can further increase the depth limit of minimally invasive skull windows.

348

12

349 **Materials and Methods**

350

351 **Adaptive optics two-photon microscopy.** A schematic diagram of our microscopy system
352 is shown in **Fig. S1**. The 2P excitation beam (920 nm) from a tunable mode-locked
353 femtosecond laser (Chameleon Ultra II, Coherent) was expanded and collimated by a pair
354 of achromatic lens to slightly overfill the aperture of the DM (DM97-15, Alpao). The
355 reflected beam with shaped wavefront was then compressed by a 4f telescope formed by
356 two VIS-NIR achromatic doublets L5 and L6 (49-365 and 49-794, Edmunds) to match the
357 aperture of a Galvo X scan mirror, which was conjugated with the DM. The Galvo XY-
358 scan mirrors (6215H, Cambridge Technology) were mutually conjugated through a 4f relay
359 formed by L7 and L8, both of which consist of two doublets (49-392, Edmunds). The Galvo
360 Y and the rear pupil of the water-immersive objective (XLPLN25XSVMP2, ×25, 1.05 NA
361 and 2mm working distance, Olympus) were then conjugated by the scan lens L9 and the
362 tube lens L10 operating in the 4f relay configuration. Two groups of scan/tube lens
363 combinations with magnification 3.33-fold or 2.25-fold were chosen to overfill or underfill
364 the objective. For the overfilled condition, L9 consists of two doublets (49-391, Edmunds)
365 and L10 is doublets (49-393, Edmund); for the underfilled condition, L9 consists of two
366 doublets (49-392, Edmunds) and L10 is changed to doublets (49-365, Edmund). The
367 objective was mounted on a motorized linear actuator (LNR50SEK1, Thorlabs) for axial
368 sectioning. For specific imaging conditions requiring two excitation wavelengths
369 simultaneously, another excitation beam (800 nm) from a tunable mode-locked
370 femtosecond laser (Mira 900, Coherent) was integrated into the microscope system via a
371 polarizing beam splitter. The system can operate in two modes: two-photon imaging and
372 wavefront sensing.

373 For two photon imaging, the epi-fluorescence collected by the objective was reflected
374 by a dichroic beam splitter D2 (FF757-Di01-25×36, Semrock) and directed to the photon
375 detection unit. An interchangeable dichroic beam splitter D3 (FF560-Di01-25×36 or
376 FF518-Di01-25X36, Semrock) was inserted at 45° to the beam path to separate the
377 fluorescence into two current photomultiplier (PMT) modules (H11461-03 and H11461-
378 01, Hamamatsu). Two band-pass filter F2 (HQ675/50M, Chroma or FF01-525/50,
379 Semrock) and F3 (FF01-525/50 or FF03-447/60, Semrock) were placed before the PMTs
380 to select the wavelength bands of the fluorescence. The PMTs current were then converted
381 to voltage by two transimpedance amplifiers (SR570, Stanford Research and DLPCA-200,
382 Femto) and subsequently fed into a multifunction data acquisition device (PCIe-6353,
383 National Instrument). Custom-written C# software running in Visual Studio (Microsoft)
384 was used to control the scanner/actuator and to acquire the TPEF images.

385 For wavefront sensing, the fluorescence emission from the guide star is transmitted
386 through another dichroic beam splitter (Di02-R488-25×36, Semrock) replacing the D2 and
387 then descanned by Galvo XY mirrors. The fluorescence signal was then reflected by the

388 DM and separated from the excitation laser by the dichroic beam splitter D1 (FF705-Di01-
389 25×36, Semrock), before being relayed by a lens pair L9 and L10(AC254-200-A and
390 AC254-100-A, Thorlabs) to the microlens array (18-00197, SUSS MicroOptics) of the
391 SHWS. The SHWS camera (iXon Ultra 888, Andor) was placed at the focal plane of the
392 microlens array to record the pattern of spots of the fluorescent guide star, enabling direct
393 measurement of its wavefront distortion. A bandpass filter F1 (HQ675/50M, Chroma or
394 FF01-525/50, Semrock) was put before the SHWS to select the wavelength of the guide
395 star signal. It should be noted that the DM, Galvo X and Y mirrors, rear pupil of the
396 objective and microlens array of SHWS were all mutually conjugated. The DM and SHWS
397 were operated in a close-loop configuration and controlled by a custom Matlab program
398 integrated with the C# imaging software.

399

400 **Calibration of the DM.** DM calibration following the previous procedure described by
401 Wang was conducted before it was integrated into the imaging system(14). Briefly, the
402 influence function of each DM actuator was measured using a Michaelson interferometer.
403 The actuators' driving voltages for the first 65 Noll's Zernike modes were then obtained
404 using the measured influence functions. After calibration, the DM can take any desired
405 shape using a linear combination of these Zernike modes.

406

407 **System AO correction.** Before any imaging experiment, the aberrations induced by the
408 optical imperfections in the microscope system were corrected based on a sensorless AO
409 algorithm(28). In brief, the TPEF intensity of a fluorescent dye (Rhodamine 6G) was used
410 as a feedback signal to optimize the DM shape pattern. Seven to nine different values for
411 each Zernike mode were applied sequentially to the DM, and the corresponding intensity
412 of fluorescence was fitted to a Gaussian function to determine the optimum value for each
413 Zernike mode. The first 21 Zernike modes (tip, tilt and defocus excluded) were used in the
414 optimization cycle to determine and compensate for the system aberration $\mathbf{Z}_{sys}$.

415

416 **Calibration of the SHWS.** The SHWS was calibrated with the DM in the microscope
417 system as described previously(16). Briefly, the nonlinear guide star from the fluorescent
418 dye solution was descanned and used for AO calibration of the DM and SHWS in a close-
419 loop configuration. The first 65 Zernike modes with root-mean-square c_i and $-c_i$ were
420 applied sequentially to the DM and the corresponding spot patterns $\mathbf{S}_i^+ =$
421 $(x_1 \cdots x_N, y_1 \cdots y_N)$ and $\mathbf{S}_i^-$ on the SHWS were recorded, where (x_j, y_j) represents the
422 center location of the j-th spots. Then the influence matrix $\mathbf{M}_{sz}$ of the DM to SHWS can
423 be acquired, where

424
$$\mathbf{M}_{sz} = \begin{bmatrix} (\mathbf{S}_1^+ - \mathbf{S}_1^-)/2c_1 \\ \vdots \\ (\mathbf{S}_{65}^+ - \mathbf{S}_{65}^-)/2c_{65} \end{bmatrix}$$

14

425   Each row of $\boldsymbol{M}_{sz}$ represent the shift (x and y) of the spots on the SHWS to each Zernike

426   mode. The 65 rows in the influence matrix $\boldsymbol{M}_{sz}$ form the calibration basis for subsequent

427   AO correction.

428

429   **Full AO correction.** Full AO correction compensates both system- and sample-induced

430   aberrations. First, the DM was set to correct the system aberration $\boldsymbol{Z}_{sys}$ obtained using the

431   sensorless method mentioned above. The TPEF signal of rhodamine at the FOV center

432   creates a reference spot pattern on the SHWS $\boldsymbol{S}_{Sref} = (x_1 \cdots x_N, y_1 \cdots y_N)$. To measure and

433   correct the sample-induced aberration, a small FOV within the sample was scanned by the

434   excitation laser to create a descanned and integrated wavefront on the SHWS. The SHWS

435   images were first cross-correlated with a Gaussian function that equals to the PSF of the

436   microlens and then the centroids of each spot were determined using a center of mass

437   algorithm with an iterative window size(33), allowing high-precision, robust estimation

438   even for asymmetric spot patterns. The reliability weight of each spot depends on its signal-

439   to-background ratio $\boldsymbol{W} = \mathrm{Diag}(w_1 \cdots w_N, w_1 \cdots w_N)$. The spot's displacement from the

440   reference pattern $\boldsymbol{S}_{Sref}$ calculated as $\Delta\boldsymbol{S} = \boldsymbol{S}_{all} - \boldsymbol{S}_{Sref}$ represents the sample-induced

441   wavefront distortion. Then the additional corrective pattern of the DM can be computed by

442   minimizing the total aberration as follows:

443     $$\Delta\boldsymbol{Z} = \arg\min_{\Delta\boldsymbol{Z}}\left\|\boldsymbol{W}^{1/2}(\boldsymbol{M}_{sz}\Delta\boldsymbol{Z} + \Delta\boldsymbol{S})\right\|^2 = -(\boldsymbol{M}_{SZ}^T\boldsymbol{W}\boldsymbol{M}_{SZ})^{-1}\boldsymbol{M}_{SZ}^T\boldsymbol{W}\Delta\boldsymbol{S}.$$

444   The corrective pattern of the DM for full AO correction is $\boldsymbol{Z}_{full} = \boldsymbol{Z}_{sys} + \Delta\boldsymbol{Z}$. Note that all

445   the corrective wavefronts shown in this work represent the corrections for sample-induced

446   aberrations.

447

448   **Direct wavefront sensing by line scanning along the microvessels in a 3D subvolume.**

449   To measure aberrations at depth, we employed the NIR guide star generated by exciting

450   Evans Blue within the microvasculature in a small 3D volume ($\sim 60\times60\times60\ \mu m^3$)). In brief,

451   we performed multiple line scans along the microvessels while integrating the guide star

452   signal on the SHWS. We repeated this procedure at two or more adjacent planes (depth

453   range < 60 µm) and obtained a series of SHWS images (**Fig. 1f-g**). Because of the large

454   optical scattering induced by the skull and brain tissue, each raw SHWS image displayed

455   distorted focus patterns in various cells of SHWS, yielding errors in aberration correction

456   (**Fig. S6**). To solve this problem, we summed all the SHWS images acquired at different

457   depths and found that the complex irregular and asymmetrical patterns were averaged out

458   in most cells. Further, for those spots with a low signal-background-ratio, we averaged

459   each cell of SHWS with its four nearest neighbors with a weight of 0.25. This wavefront

460   reconstruction algorithm yields a high-quality SHWS image and a single focus stands out

461   in each cell, allowing more accurate determination of the average aberrations in the

462   scattering biological samples (**Fig. S6**).

15

463

464   **Animal preparation.** Four transgenic mouse lines: Thy1-YFP (Tg(Thy1-

465   YFP)HJrs/J)(34), Cx3Cr1-GFP (B6.129P2(Cg)-Cx3cr1^{tm1Litt}/J)(35), Thy1-YFP/Cx3Cr1-

466   GFP and APP-PS1/Cx3Cr1-GFP were used in this study. Thy1-YFP/Cx3Cr1-GFP mice

467   were generated by crossing Thy1-YFP mice with Cx3Cr1-GFP mice, and APP-

468   PS1/Cx3Cr1-GFP mice were obtained by crossing APP-PS1 (Tg

469   (APPswe,PSEN1dE9)85Dbo) mice with Cx3Cr1-GFP mice. All the animal procedures

470   conducted in this work followed an animal protocol approved by the Animal Ethics

471   Committee of HKUST.

472   Mice (>6 weeks) were anesthetized by intraperitoneal (i.p.) injection of

473   ketamine/xylazine mixture (10µL/g) before surgery. After the skull was exposed by

474   performing a midline scalp incision, a scalpel was used to remove gently the periosteum

475   attached to the skull. Then a custom-designed rectangular head plate with a circular hole

476   was centered on the right hemisphere and sealed onto the skull by applying a small amount

477   of cyanoacrylate adhesive to the perimeter of the hole. Dental acrylic was then applied to

478   the exposed skull surface to fill the gap between the head plate and skull. After the dental

479   acrylic became dry and hard, the mice were mounted on a head-holding stage with angle

480   adjusters (NARISHIGE, MAG-2) and placed under a stereomicroscope for surgical

481   preparation of either a thinned skull or optical-cleared skull window.

482

483   *Thinned skull window.* The thinned skull preparation is slightly modified from a previous

484   protocol(4). Briefly, a 500-µm carbon steel burr attached to a rotary high-speed drill was

485   used to gently thin a circular region (2.0-2.5mm in diameter) with the center at stereotactic

486   coordinate (3mm, 3mm) laterally and posterior to the bregma point. After removing the

487   majority of the middle spongy bone, a micro surgical blade (no. 6961, Surgistar) was used

488   to carefully thin the skull further to about 40-50 µm. Surface irregularities were reduced

489   by occasionally changing the thinning direction of the surgical blade. Finally, a

490   biocompatible sealant mixture (Kwik-Cast, WPI) which can be peeled off before the

491   imaging experiment was applied to cover the thinned skull window.

492

493   *Optical clearing skull window.* The reagents used for optically clearing the skull include:

494   10% EDTA disodium (D2900000, Sigma-Aldrich), 80% glycerol (G5516, Sigma-Aldrich)

495   and USOCA (consists of S1 and S2)(7–9). S1 is prepared by dissolving urea (Sinopharm,

496   China) in 75% ethanol at a 10:3 volume-mass ratio. S2 is a sodium

497   dodecylbenzenesulfonate (SDBS) prepared by mixing NaOH solution (0.7 M) with

498   dodecylbenzenesulfonic acid (DDBSA, Aladdin) at a 24:5 volume-mass ratio. The skull

499   optical clearing procedure follows the method described in previous reports(7–9). Briefly,

500   the exposed skull was first treated with S1 for about 20 min, with a clean cotton swab

501   gently rubbing the skull surface to accelerate the clearing process. Then the S1 was

502   removed using a cotton ball and replaced with S2 for a further 5 min. After the S2 was
503   removed, 10% EDTA was dropped onto the skull for another 20 min and then replaced
504   with 80% glycerol. Finally, a thin layer of plastic wrap was used to cover the cleared skull
505   to separate the immersion medium (water) from glycerol during *in vivo* imaging.

506

507   ***In vivo* imaging.** Mice were anesthetized with ketamine/xylazine and received a retro-
508   orbital intravenous injection of Evans Blue (10ug/g; E2129, Sigma-Aldrich) 30 minutes
509   before imaging to label the lumen of blood vessels. The APP-PS1/Cx3Cr1-GFP mice were
510   also i.p. injected with MeO-X04 (5.0 mg/kg, 10% DMSO, 90% PBS) 2 hours before
511   imaging to label amyloid deposits in the brain. Before fluorescence imaging, the skull
512   window was aligned precisely perpendicular to the objective axis by adjusting the angles
513   of the head-holding stage guided by second-harmonic generation imaging of bone collagen.
514   For two-photon imaging of neurons (YFP), microglia (GFP) and blood vessels (Evans
515   Blue), the femtosecond laser was tuned to 920 nm and the post-objective excitation power
516   ranged from 20-200 mW depending on the imaging depth. To image amyloid plaques in
517   the APP-PS1/Cx3Cr1-GFP mice, another femtosecond laser tuned to 800 nm was used to
518   excite the MeO-X04 fluorescence with an incident power of less than 30mW at the skull
519   surface. For wavefront sensing, the nonlinear fluorescence guide star was created by
520   scanning the 920 nm laser over a small FOV ($30\times30\mu m^2$) or selectively choosing a small
521   vessel via multiple line scanning. Detailed imaging and wavefront sensing parameters are
522   listed in **Table S1**.

523

524   **Laser-mediated microsurgery.** To perform precise and efficient microsurgery using the
525   femtosecond laser, the sample-induced aberration for the ablation site was first measured
526   and compensation applied. For laser dendrotomy, a 920 nm laser with an average power of
527   400 mW was focused on the dendritic shaft for 1-2s, the actual exposure time being
528   controlled by the feedback signal of newly-created fluorescence during the multiphoton
529   ionization process(36, 37). For single spine ablation, a 920 nm laser with an average power
530   of 200-300 mW was focused on the dendritic spine for 2s.

531

532   **Spectra unmixing of GFP and YFP signal.** We used Thy1-YFP/Cx3Cr1-GFP mice to
533   study the interaction between neurons and microglia. Because the emission spectra of YFP
534   and GFP are very close, we designed a simple algorithm using a linear model to distinguish
535   the two components. To image GFP and YFP, D3 was replaced with dichroic beam splitter
536   FF518-Di01-25X36 and F2 and F3 were both the band-pass filter FF01-525/50 (**Fig. S1**).
537   Therefore, the detection bands of the two PMT channels are 518-550 nm and 500-518 nm
538   respectively, corresponding to the emission peaks of YFP and GFP. Assuming that the
539   fluorescence brightness of YFP and GFP at the imaging location are C_Y and C_G, and the

540 detected signal intensities of PMT1 and PMT2 are I_1 and I_2, we have the following
541 equations:

$$\begin{bmatrix} I_1 \\ I_2 \end{bmatrix} = \begin{bmatrix} w_{1,1} & w_{1,2} \\ w_{2,1} & w_{2,2} \end{bmatrix} \begin{bmatrix} C_Y \\ C_G \end{bmatrix} = \begin{bmatrix} w_1 & 1 \\ 1 & w_2 \end{bmatrix} \begin{bmatrix} \alpha C_Y \\ \beta C_G \end{bmatrix}$$

543 The parameters w_1 and w_2 can be calibrated from the image locations where only YFP
544 labelled neurons or GFP labelled microglia exist. The unmixed normalized signal intensity
545 for YFP and GFP can be represented by αC_Y and βC_G, where:

$$\begin{bmatrix} \alpha C_Y \\ \beta C_G \end{bmatrix} = \begin{bmatrix} w_1 & 1 \\ 1 & w_2 \end{bmatrix}^{-1} \begin{bmatrix} I_1 \\ I_2 \end{bmatrix}$$

547 By using this method, we can unmix the fluorescence signal of YFP-labelled neurons and
548 GFP-labelled microglia.

549

550 **Image analysis.** The images were processed in Matlab (Mathworks) or ImageJ (NIH)(38).
551 Several algorithms for images registration were used to mitigate motion artifacts depending
552 on the level of the animal motion itself. For most imaging conditions when the animal
553 motion was negligible, only a single frame was captured per slice for the stack images. The
554 stack images were registered using the rigid-body transformation provided by the stackreg
555 plugin(39) in ImageJ. When animal motion became apparent and inter-frame artifacts
556 appeared, the imaging speed was increased and several frames were acquired per slice for
557 the whole stack images (**Table S1**). Image registration was performed on sequential frames
558 for each slice using the turboreg plugin(39) in ImageJ to correct the rigid motion artifact,
559 or with the hidden Markov model algorithm(40) to correct within-frame motion artifacts.
560 For mosaiced images of microglia and blood vessel, multi-tile subimages were captured
561 with predefined positions and then stitched together to form the mosaic image using the
562 Grid/Collection Stitching(41) plugin in ImageJ.

563

564 **Acknowledgments**

571

572 **Author contributions**

573 C.C., Z.Q., D.Z., N.Y.I. and J.Y.Q. conceived of the research idea. C.C. and Z.Q. designed
574 and conducted the experiments and data analysis. Z.Q., S.H. and C.C. built the AO two-

18

575 photon imaging system. C.C. carried out the surgery with the assistance of S.L., S.F.L. and
576 W.W.. Finally, Z.Q. and C.C. took the lead in writing the manuscript with inputs from all
577 other authors.
578
579 **Competing interests**

580 All authors declare that they have no competing interests.
581

582 **References**
583

584 1. F. Helmchen, W. Denk, Deep tissue two-photon microscopy. *Nat. Methods* **2**, 932–
585   940 (2005).

586 2. K. Svoboda, R. Yasuda, Principles of two-photon excitation microscopy and its
587   applications to neuroscience. *Neuron* **50**, 823–839 (2006).

588 3. A. Holtmaat, *et al.*, Long-term, high-resolution imaging in the mouse neocortex
589   through a chronic cranial window. *Nature Protocols* **4**, 1128–1144 (2009).

590 4. G. Yang, F. Pan, C. N. Parkhurst, J. Grutzendler, W.-B. Gan, Thinned-skull cranial
591   window technique for long-term imaging of the cortex in live mice. *Nat Protoc* **5**,
592   201–208 (2010).

593 5. H.-T. Xu, F. Pan, G. Yang, W.-B. Gan, Choice of cranial window type for *in vivo*
594   imaging affects dendritic spine turnover in the cortex. *Nature Neuroscience* **10**, 549–
595   551 (2007).

596 6. C. Chen, *et al.*, In Vivo Near-Infrared Two-Photon Imaging of Amyloid Plaques in
597   Deep Brain of Alzheimer's Disease Mouse Model. *ACS Chem. Neurosci.* **9**, 3128–
598   3136 (2018).

599 7. Y.-J. Zhao, *et al.*, Skull optical clearing window for *in vivo* imaging of the mouse
600   cortex at synaptic resolution. *Light: Science & Applications* **7**, 17153 (2018).

601 8. C. Zhang, *et al.*, A large, switchable optical clearing skull window for cerebrovascular
602   imaging. *Theranostics* **8**, 2696–2708 (2018).

603 9. Y. Chen, *et al.*, Coherent Raman Scattering Unravelling Mechanisms Underlying
604   Skull Optical Clearing for Through-Skull Brain Imaging. *Anal. Chem.* **91**, 9371–9375
605   (2019).

606 10. M. J. Booth, Adaptive optical microscopy: the ongoing quest for a perfect image.
607   *Light: Science & Applications* **3**, e165 (2014).

608 11. N. Ji, Adaptive optical fluorescence microscopy. *Nature Methods* **14**, 374–380
609   (2017).

610 12. R. Aviles-Espinosa, *et al.*, Measurement and correction of in vivo sample aberrations
611   employing a nonlinear guide-star in two-photon excited fluorescence microscopy.
612   *Biomed. Opt. Express, BOE* **2**, 3135–3149 (2011).

613 13. K. Wang, *et al.*, Rapid adaptive optical recovery of optimal resolution over large
614   volumes. *Nature Methods* **11**, 625–628 (2014).

615 14. K. Wang, *et al.*, Direct wavefront sensing for high-resolution in vivo imaging in
616   scattering tissue. *Nature Communications* **6**, 7276 (2015).

617 15. R. Liu, Z. Li, J. S. Marvin, D. Kleinfeld, Direct wavefront sensing enables functional
618   imaging of infragranular axons and spines. *Nat Methods* **16**, 615–618 (2019).

619 16. Z. Qin, *et al.*, Adaptive optics two-photon microscopy enables near-diffraction-
620   limited and functional retinal imaging in vivo. *Light Sci Appl* **9**, 79 (2020).

621 17. D. Débarre, *et al.*, Image-based adaptive optics for two-photon microscopy. *Optics*
622   *letters* **34**, 2495–2497 (2009).

623 18. N. Ji, D. E. Milkie, E. Betzig, Adaptive optics via pupil segmentation for high-
624   resolution imaging in biological tissues. *Nature Methods* **7**, 141–147 (2010).

625 19. J. Tang, R. N. Germain, M. Cui, Superpenetration optical microscopy by iterative
626   multiphoton adaptive compensation technique. *Proceedings of the National Academy*
627   *of Sciences* **109**, 8434–8439 (2012).

628 20. M. Kondo, K. Kobayashi, M. Ohkura, J. Nakai, M. Matsuzaki, Two-photon calcium
629   imaging of the medial prefrontal cortex and hippocampus without cortical invasion.
630   *eLife* **6**, e26839 (2017).

631 21. C. N. Parkhurst, W.-B. Gan, Microglia dynamics and function in the CNS. *Current*
632   *Opinion in Neurobiology* **20**, 595–600 (2010).

633 22. C. Madry, *et al.*, Microglial Ramification, Surveillance, and Interleukin-1β Release
634   Are Regulated by the Two-Pore Domain K + Channel THIK-1. *Neuron* **97**, 299-
635   312.e6 (2018).

636 23. R. A. Armstrong, Original article Laminar distribution of β-amyloid (Aβ) peptide
637   deposits in the frontal lobe in familial and sporadic Alzheimer's disease. *fn* **1**, 15–23
638   (2015).

24. L. Sacconi, *et al.*, In vivo multiphoton nanosurgery on cortical neurons. *Journal of Biomedical Optics* **12**, 050502 (2007).

25. A. J. Canty, *et al.*, In-vivo single neuron axotomy triggers axon regeneration to restore synaptic density in specific cortical circuits. *Nature Communications* **4** (2013).

26. N. Nishimura, *et al.*, Targeted insult to subsurface cortical blood vessels using ultrashort laser pulses: three models of stroke. *Nature Methods* **3**, 99–108 (2006).

27. A. Y. Shih, *et al.*, The smallest stroke: occlusion of one penetrating vessel leads to infarction and a cognitive deficit. *Nature Neuroscience* **16**, 55–63 (2013).

28. J.-H. Park, L. Kong, Y. Zhou, M. Cui, Large-field-of-view imaging by multi-pupil adaptive optics. *Nature Methods* **14**, 581–583 (2017).

29. T. Wang, *et al.*, Three-photon imaging of mouse brain structure and function through the intact skull. *Nature Methods* (2018) https:/doi.org/10.1038/s41592-018-0115-y (September 24, 2018).

30. D. M. Chow, *et al.*, Deep three-photon imaging of the brain in intact adult zebrafish. *Nature Methods*, 1–4 (2020).

31. O. T. Bruns, *et al.*, Next-generation in vivo optical imaging with short-wave infrared quantum dots. *Nat Biomed Eng* **1** (2017).

32. S. Wang, J. Liu, G. Feng, L. G. Ng, B. Liu, NIR-II Excitable Conjugated Polymer Dots with Bright NIR-I Emission for Deep In Vivo Two-Photon Brain Imaging Through Intact Skull. *Advanced Functional Materials* **29**, 1808365 (2019).

33. P. M. Prieto, F. Vargas-Martín, S. Goelz, P. Artal, Analysis of the performance of the Hartmann–Shack sensor in the human eye. *J. Opt. Soc. Am. A, JOSAA* **17**, 1388–1398 (2000).

34. G. Feng, *et al.*, Imaging neuronal subsets in transgenic mice expressing multiple spectral variants of GFP. *Neuron* **28**, 41–51 (2000).

35. S. Jung, *et al.*, Analysis of Fractalkine Receptor CX3CR1 Function by Targeted Deletion and Green Fluorescent Protein Reporter Gene Insertion. *Mol Cell Biol* **20**, 4106–4114 (2000).

667   36.   Q. Sun, *et al.*, In vivo imaging-guided microsurgery based on femtosecond laser
668   produced new fluorescent compounds in biological tissues. *Biomed. Opt. Express,*
669   *BOE* **9**, 581–590 (2018).

670   37.   Z. Qin, *et al.*, New fluorescent compounds produced by femtosecond laser surgery in
671   biological tissues: the mechanisms. *Biomedical Optics Express* **9**, 3373 (2018).

672   38.   J. Schindelin, *et al.*, Fiji: an open-source platform for biological-image analysis.
673   *Nature Methods* **9**, 676–682 (2012).

674   39.   P. Thévenaz, U. E. Ruttimann, M. Unser, A pyramid approach to subpixel registration
675   based on intensity. *IEEE Trans Image Process* **7**, 27–41 (1998).

676   40.   P. Kaifosh, M. Lovett-Barron, G. F. Turi, T. R. Reardon, A. Losonczy, Septo-
677   hippocampal GABAergic signaling across multiple modalities in awake mice. *Nature*
678   *Neuroscience* **16**, 1182–1184 (2013).

679   41.   S. Preibisch, S. Saalfeld, P. Tomancak, Globally optimal stitching of tiled 3D
680   microscopic image acquisitions. *Bioinformatics* **25**, 1463–1465 (2009).

681

682

683 **Supplementary Figures**

684
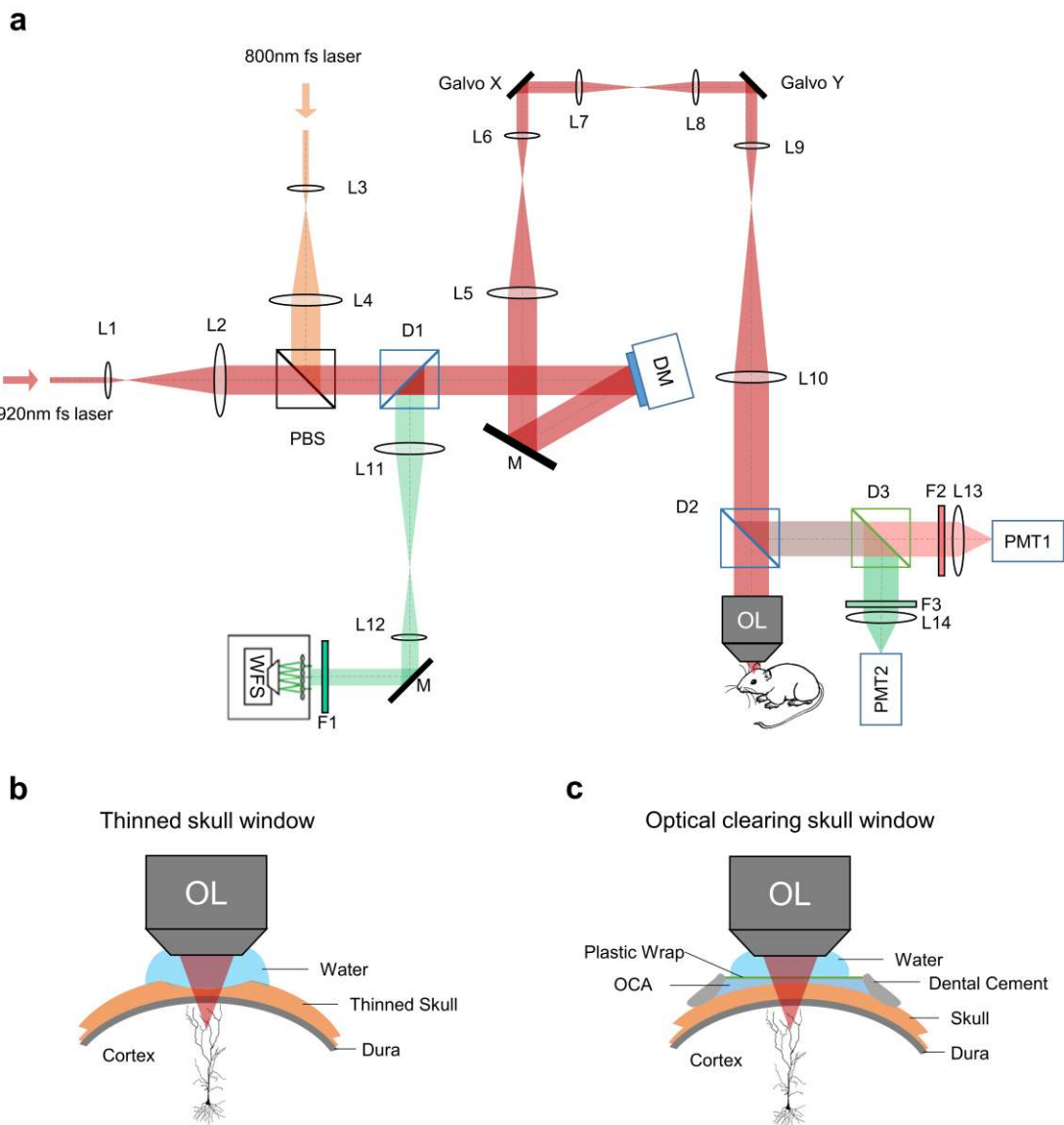

685
686 **Fig. S1. Schematic diagrams of our AO two-photon microscope system and minimally invasive skull**
687 **windows.** (a) Schematic of adaptive optics two-photon microscope setup. L1-L14: lenses; OL: objective
688 lens; D1-D3: dichroic mirrors; F1-F3: filters; M: mirrors; DM: deformable mirror; WFS: wavefront sensor;
689 PMT1-2: photomultiplier tubes. (b) Schematic of thinned skull window. (c) Schematic of optical clearing
690 skull window. OCA: optical clearing agents.
691
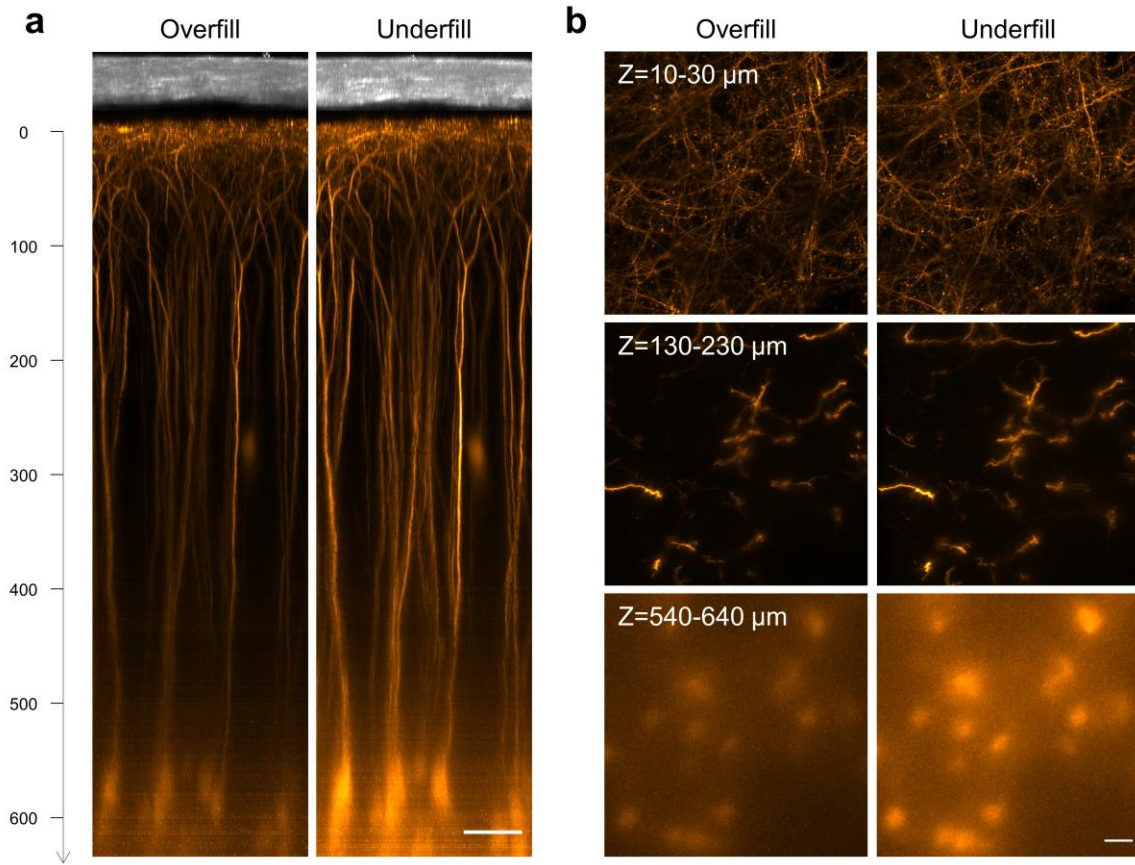
692
693
694 **Fig. S2. The use of an underfilled objective improved the excitation efficiency for transcranial deep**
695 **brain imaging.** (a) xz maximum-intensity projection (MIP) images of the pyramidal neurons in Thy1-YFP
696 mice through a 50-µm-thickness thinned-skull window acquired using the overfilled (left) and underfilled
697 (right) objective. The imaging conditions including excitation power, pixel size and frame rate were
698 identical at the same depth for both configurations. Scale bar: 50 µm. (b) xy MIP (top row: 10-30µm;
699 middle row: 120-230 µm; bottom row: 540-640 µm) of the images in (a). Scale bar: 20 µm.
700
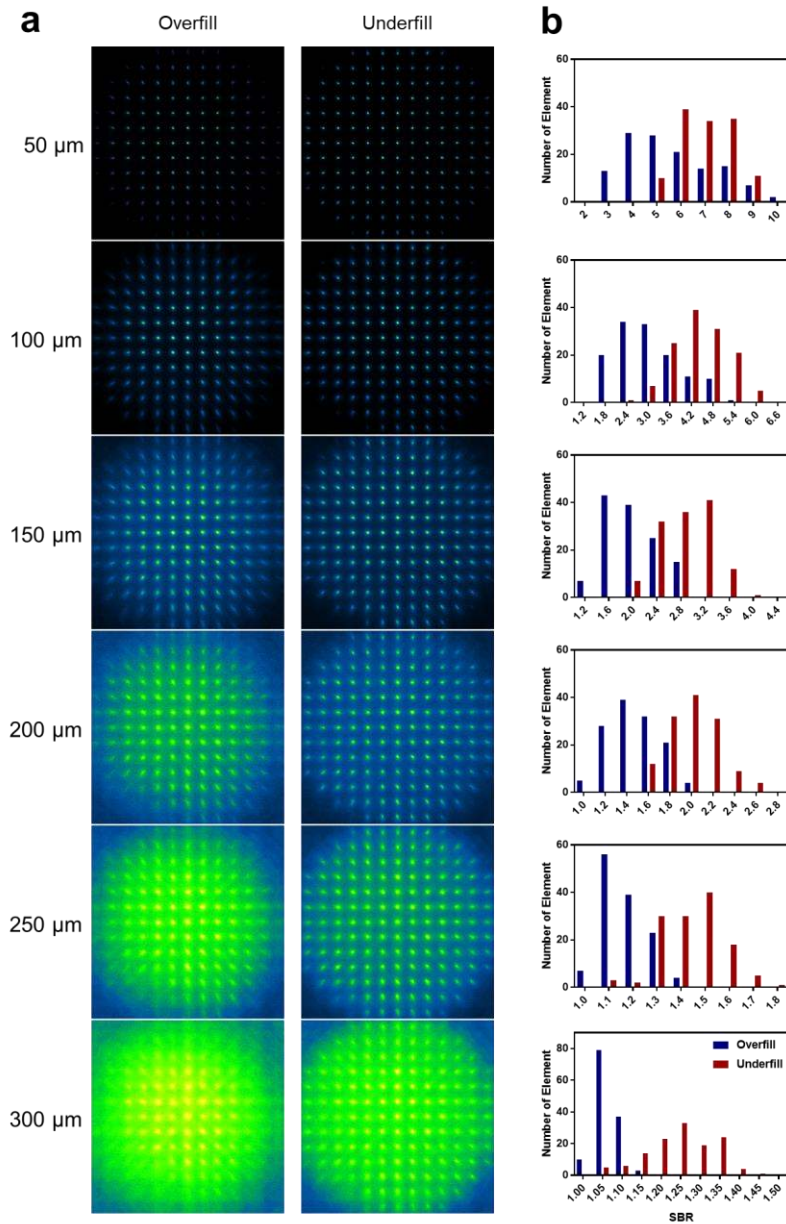
Fig. S3. Comparison of guide star images on SHWS using an overfilled or underfilled objective. (a) Guide star images of YFP fluorescence in Thy1-YFP mice when the objective was overfilled (left column) and underfilled (right column) at different depths below the thinned skull. The guide star images were measured at the same location as Fig. S2a. (b) Histograms of the signal-to-background ratio (SBR) of the guide star images at different depths when the objective was underfilled (red) and overfilled (blue). The total element number of the SHWS is 129. The total element number of the SHWS is 129. The SBR was defined by the average intensity of 4×4 pixels around the spots center to that of the remaining pixels in each cell of SHWS. We found that when the SBR was less than 1.2, the fitting of spot center would be inaccurate and thus that spot was defined as a bad spot.
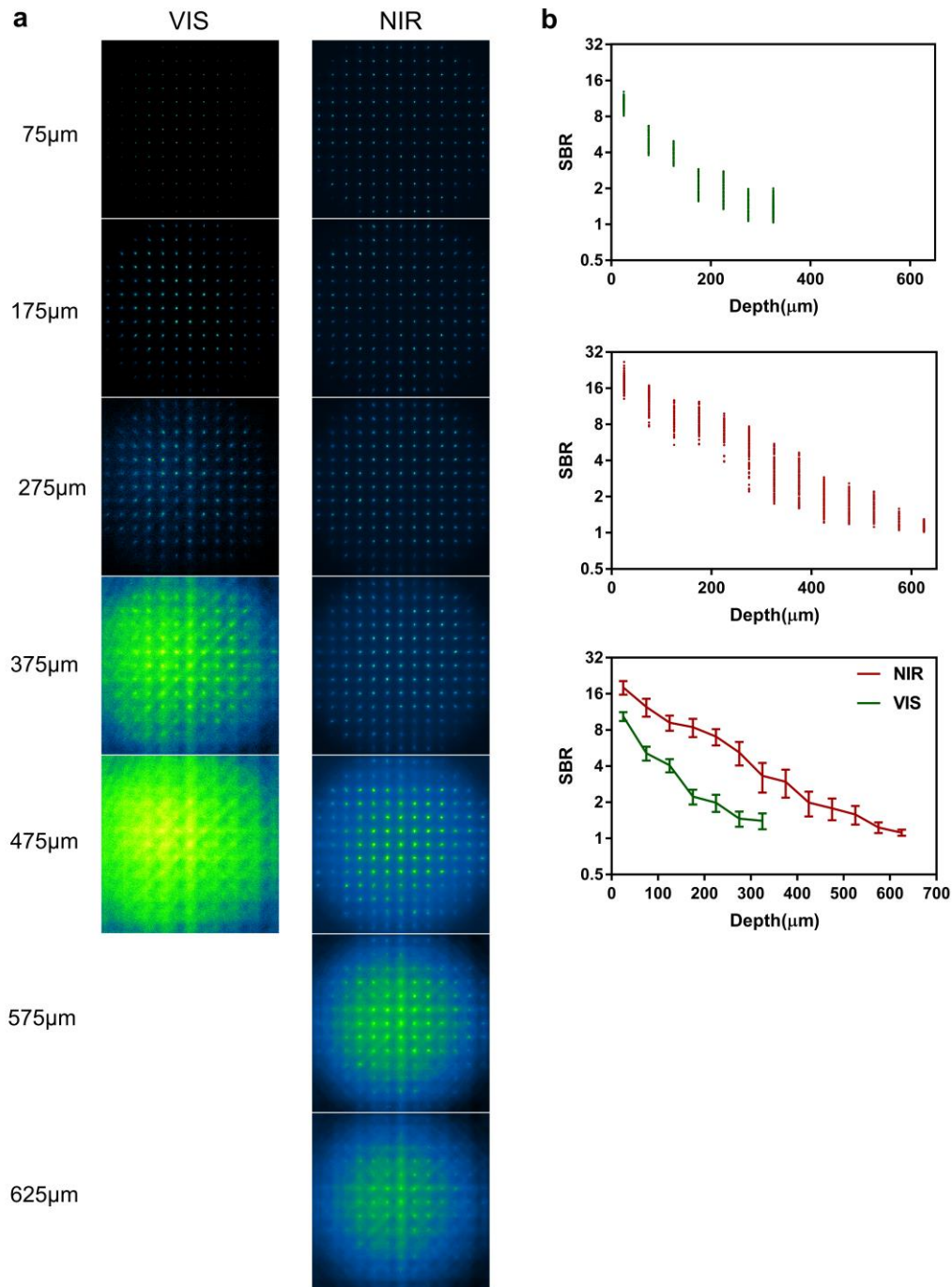
Fig. S4. Comparison of the visible and NIR guide star generated by two-photon excitation of YFP and Evans blue in the mouse cortex through a thinned-skull window. (a) Typical guide star images on SHWS at different depths by two-photon excitation of YFP labelled pyramidal neurons (left) and Evans blue labelled microvessels (right) at the same location. (b) The signal-to-background ratio of the visible and NIR guide star.
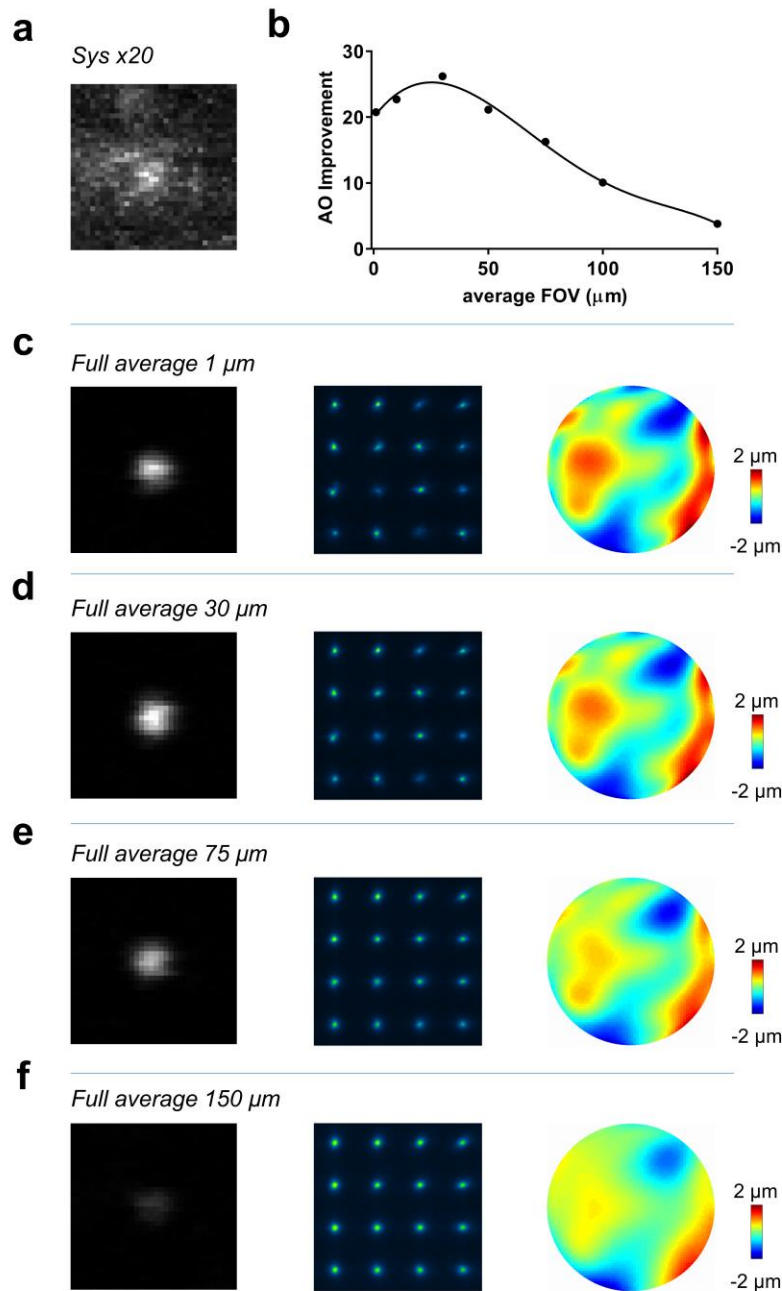
720
721
Fig. S5. Characterization of the AO corrective FOV through a thinned-skull window. (a) xy MIP image of a 200-nm-diameter bead 400 µm beneath the thinned-skull (50 µm in thickness) with system correction alone. The image brightness was enhanced 20-fold to visualize the details. (b) Improvement of fluorescence intensity of the bead located at the FOV center by AO correction with guide star signals averaged over a square field ranging from 1 µm to 150 µm per side. (c-f) AO corrected xy MIP images of the fluorescent beads (left column), corresponding guide star images (middle column) and corrective wavefront (right column) when the guide star signal is averaged over 1 µm (c), 30 µm (d), 75 µm (e) and 150 µm(f).
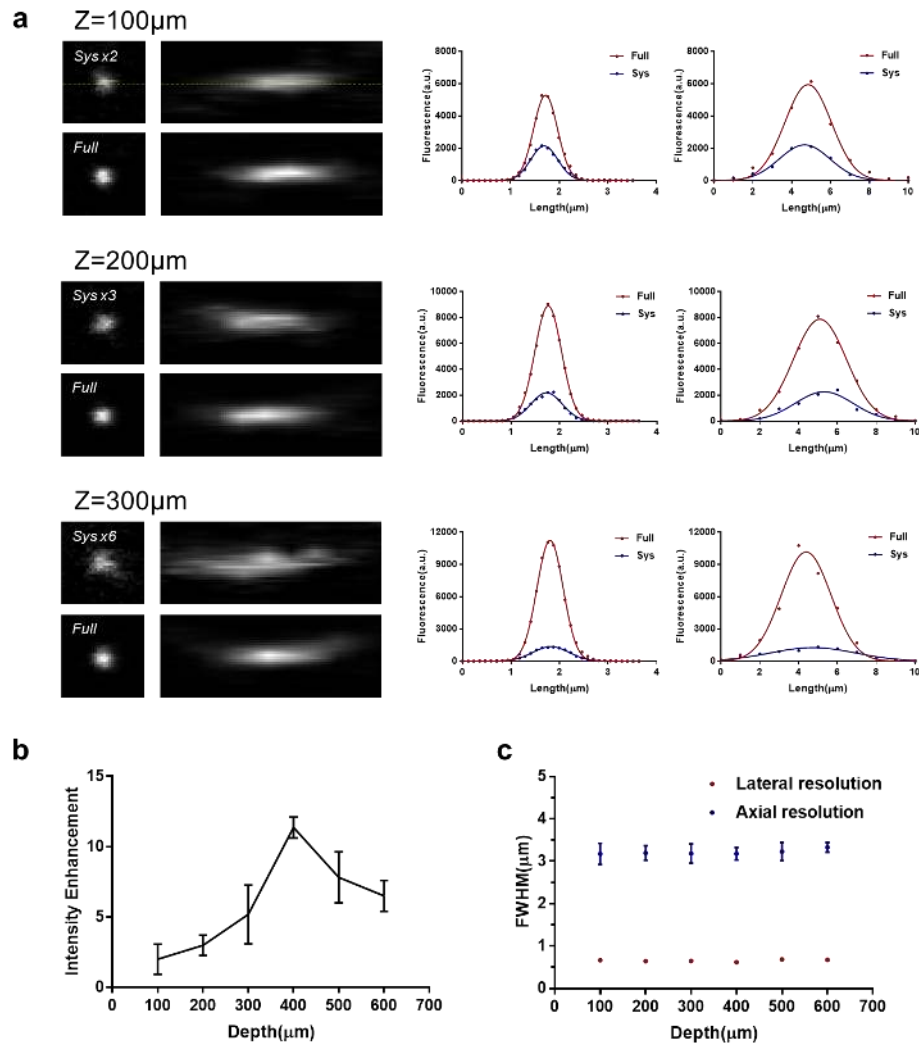
Fig. S6. *In vitro* characterization of aberrations of a thinned-skull window. (a) Left column: lateral and axial PSF measured with 200 nm diameter fluorescent beads at different depths with system and full AO correction. The images with system correction were enhanced to visualize details. Middle column: lateral intensity profile along the dashed line with system (blue) and full (red) AO correction. Right column: axial intensi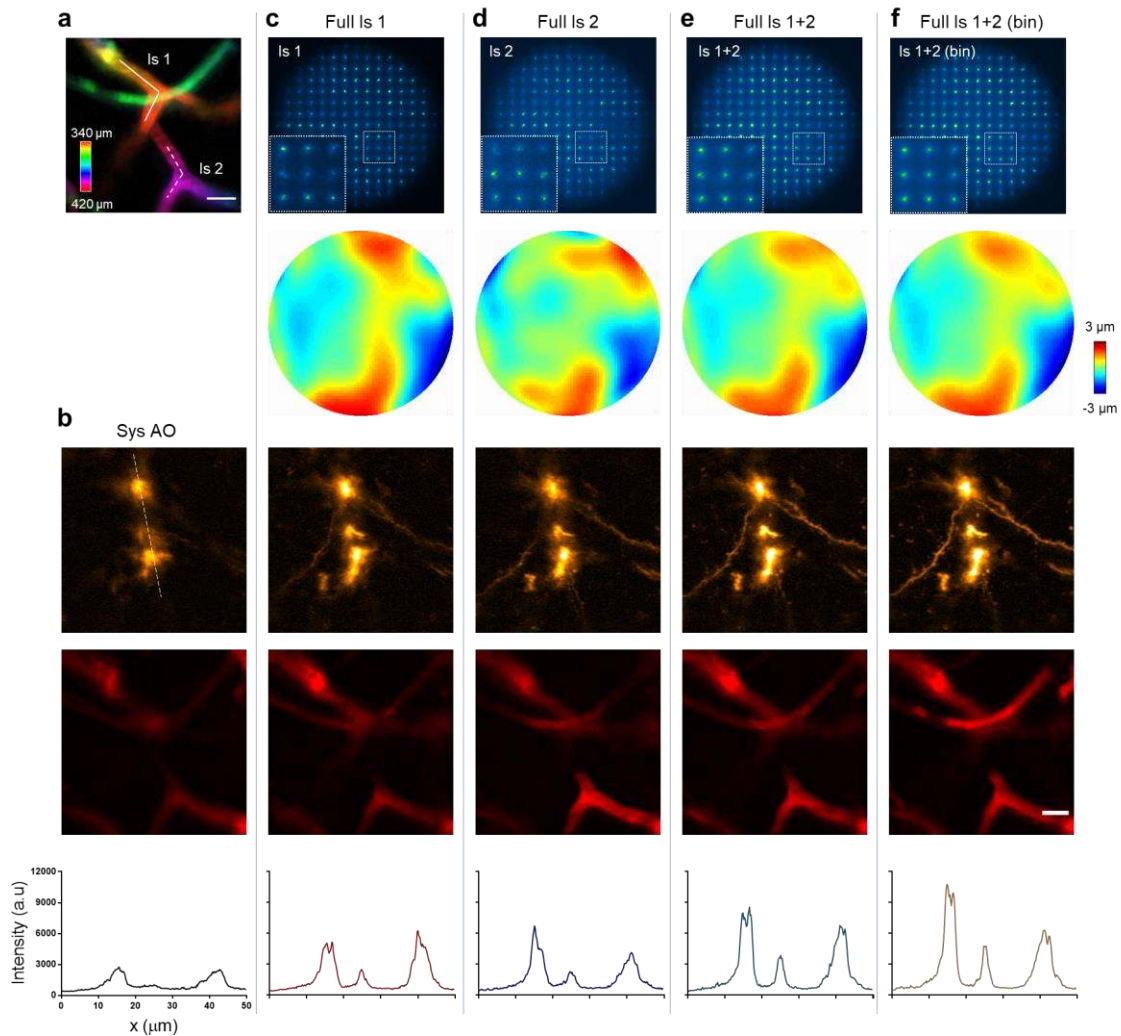ty profile with system and full AO correction. Full AO correction was performed by averaging the guide star signal over 30×30 µm². (b) The improvement of fluorescence intensity by full AO correction at different depths. (c) The lateral (red) and axial (blue) resolution after full AO correction.

Fig. S7. Direct wavefront sensing algorithm for through-skull imaging of the brain. (a) 3D distribution of the vasculature for direct wavefront sensing using a NIR guide star. Two segments of vessels (solid line and dashed line labelled with ls 1 and ls 2) at different depths were line scanned for wavefront measurement. (b) xy MIP images (Z = 340-420 µm) of neuron (top) and microvasculature (middle) and intensity profile along the dashed line (bottom) with only system aberrations corrected. (c-f) 1st row: guide star images on the SHWS, the inset shows a magnified view of the box region; 2nd row: the corresponding corrective wavefront on the DM; 3rd row: MIP images of neurons after correction; 4th row: MIP images of microvessels after correction; 5th row: intensity profile along the dashed line in (top panel of (b)). The AO corrections in (c-f) were based on direct wavefront measurement with only ls 1 (c) or ls 2 (d), the sum of ls 1 and ls 2 (e) and our algorithm by summing ls 1 and ls 2 and subsequent filtering (f).
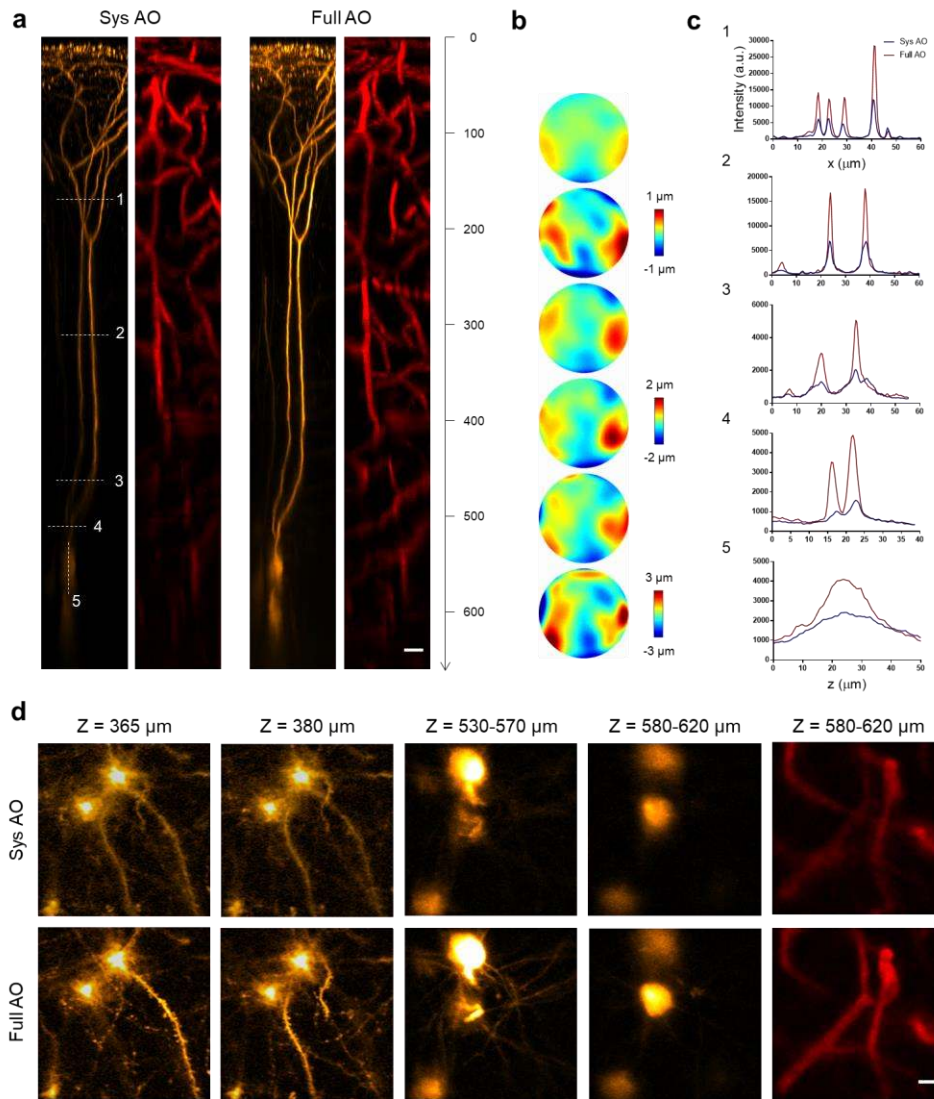
Fig. S8. AO recovers high-resolution imaging of the cortex through a thinned-skull window. (a) xz MIP images of the pyramidal neurons (orange) and microvasculature (red) in Thy1-YFP mice through a thinned-skull window (50 µm in thickness) with system correction only (left) and full AO correction (right). AO correction was performed every 50 µm deep. Scale bar: 20 µm. (b) Representative corrected wavefront of the DM at depths (Z = 100, 200, 300, 400, 500 and 600 µm) used in (a). (c) The intensity profile of the dashed line in (a) with system (blue) and full (red) AO correction. (d) xy MIP of the stack images in (a). Orange: neuron; red: microvasculature. Scale bar: 10 µm.
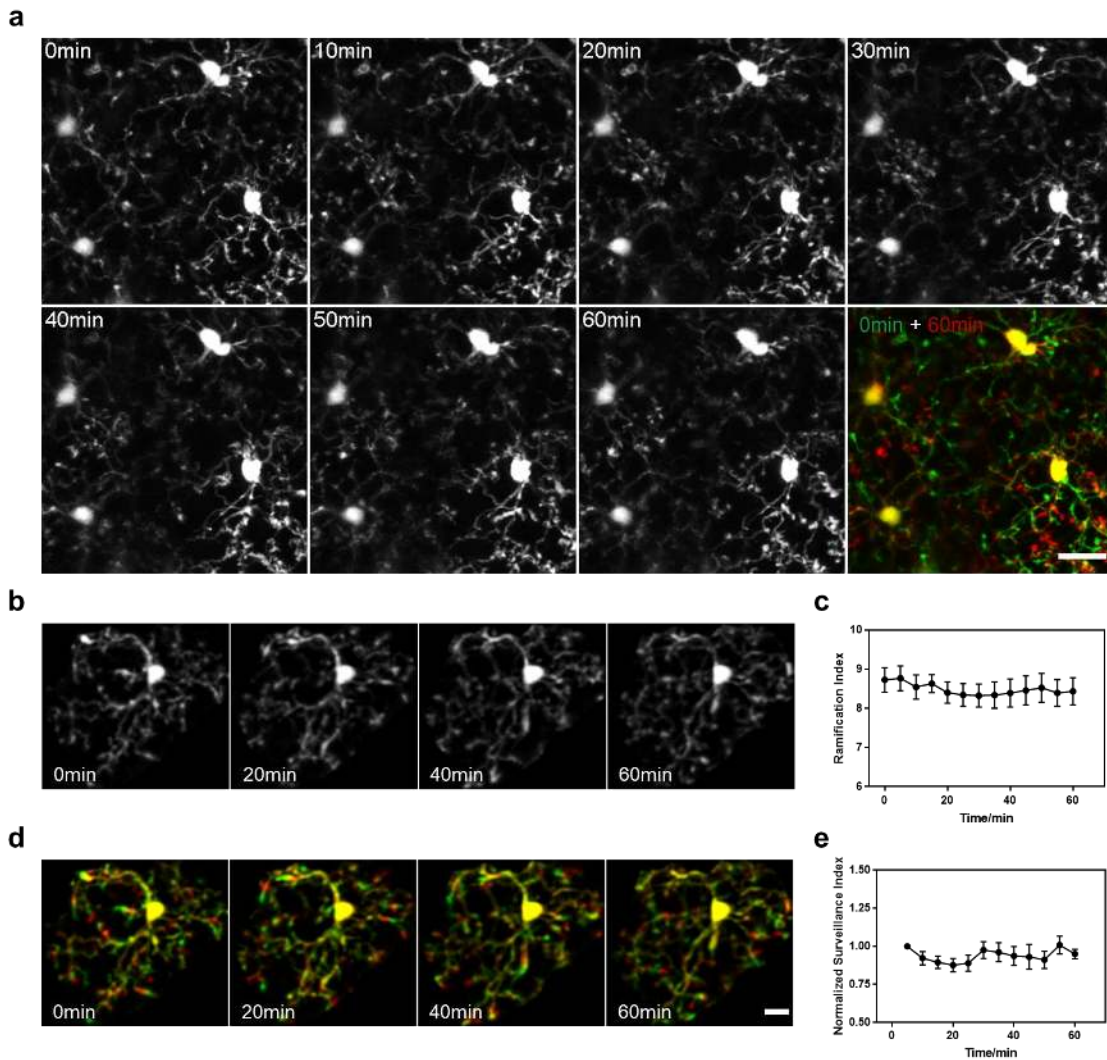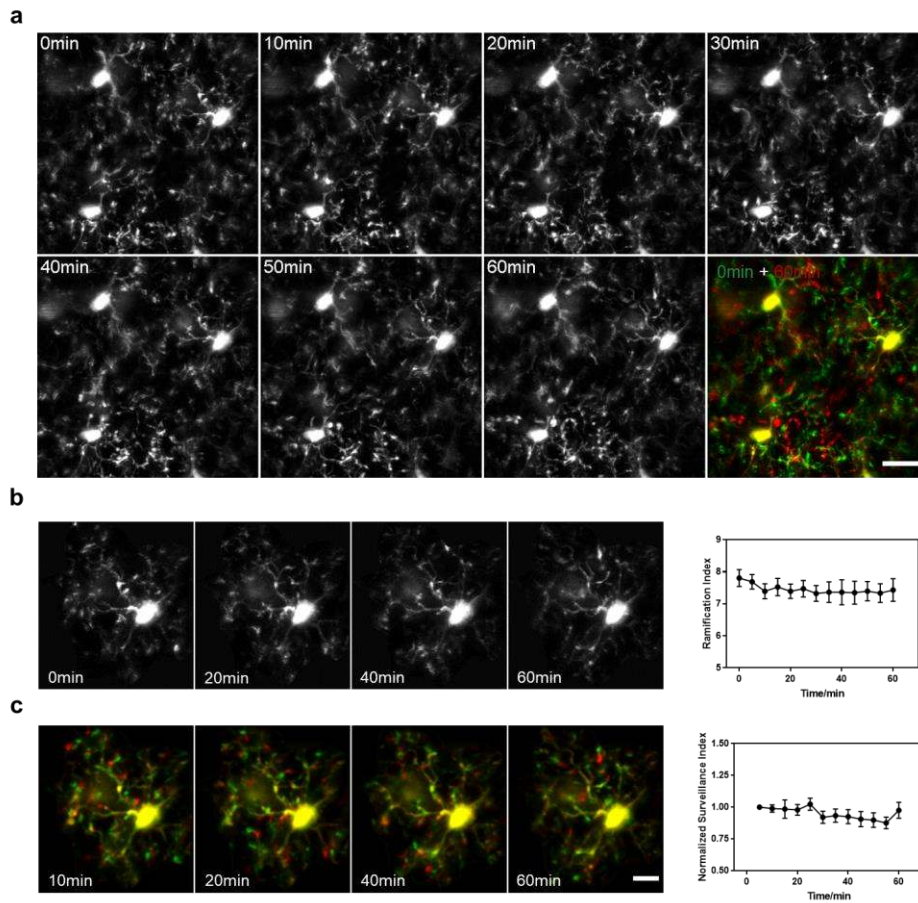
Fig. S9. Investigation of microglial inflammation of a thinned-skull window. (a) Time-lapse images showing that microglia remain stable after preparing the thinned-skull. Scale bar: 20 µm. (b) Representative magnified images showing that microglia remain highly ramified under the thinned-skull window. (c) Changes in the microglial ramification index at different times. (d) Merged images (green and red) of two consecutive time points at 5 min interval, showing microglial process movement during surveillance (green: retracted, red: extended) at different times. Scale bar: 10 µm. (e) Changes of microglial surveillance index at different times. Data were normalized to initial time point.
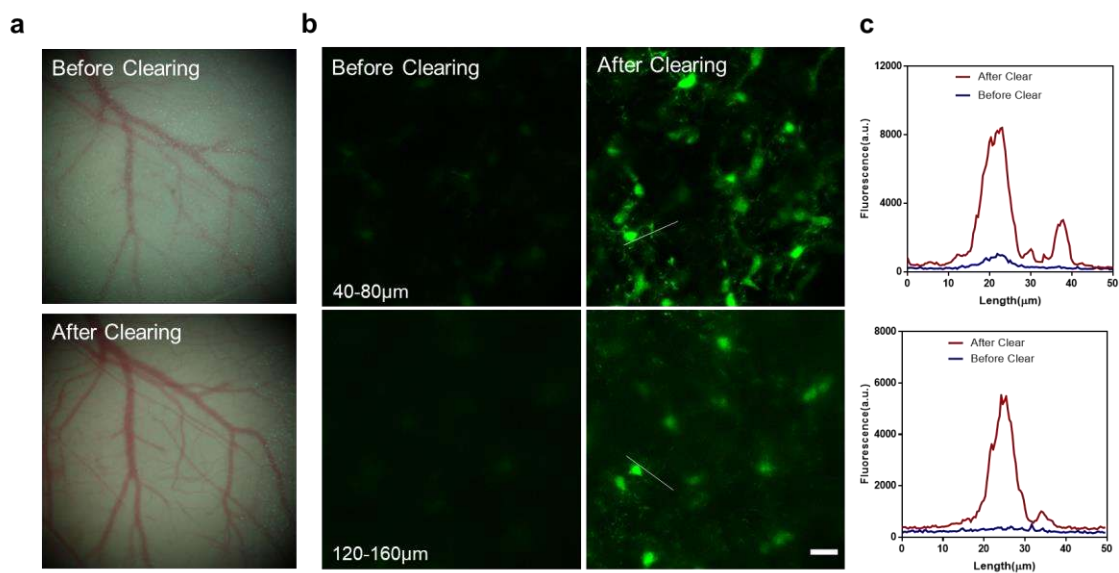
770
771
Fig. S10. *In vivo* **imaging of the brain through an optical clearing window**. (a) Bright-field image
before (top) and after (bottom) optical clearing. (b) xy MIP of a two-photon image of the GFP labelled
microglial in the Cx3Cr1-GFP mice before (left column) and after (right column) optical clearing. Imaging
depths: top row: Z = 40-80 µm; bottom row: Z = 120-160 µm. (c) Intensity profile along the lines in (b).
776

Fig. S11. Investigation of microglial inflammation of an optical clearing window. (a) Time-lapse images showing that microglia remain stable after optical clearing of the skull. Scale bar: 20 µm. (b) Representative magnified images showing that microglia remain highly ramified under the thinned-skull window. (c) Changes in the microglial ramification index at different times. (d) Merged images (green and red) of two consecutive time points at 5 min interval, showing microglial process movement during surveillance (green: retracted, red: extended) at different times. Scale bar: 10 µm. (e) Changes of microglial surveillance index at different times. Data were normalized to initial time point.

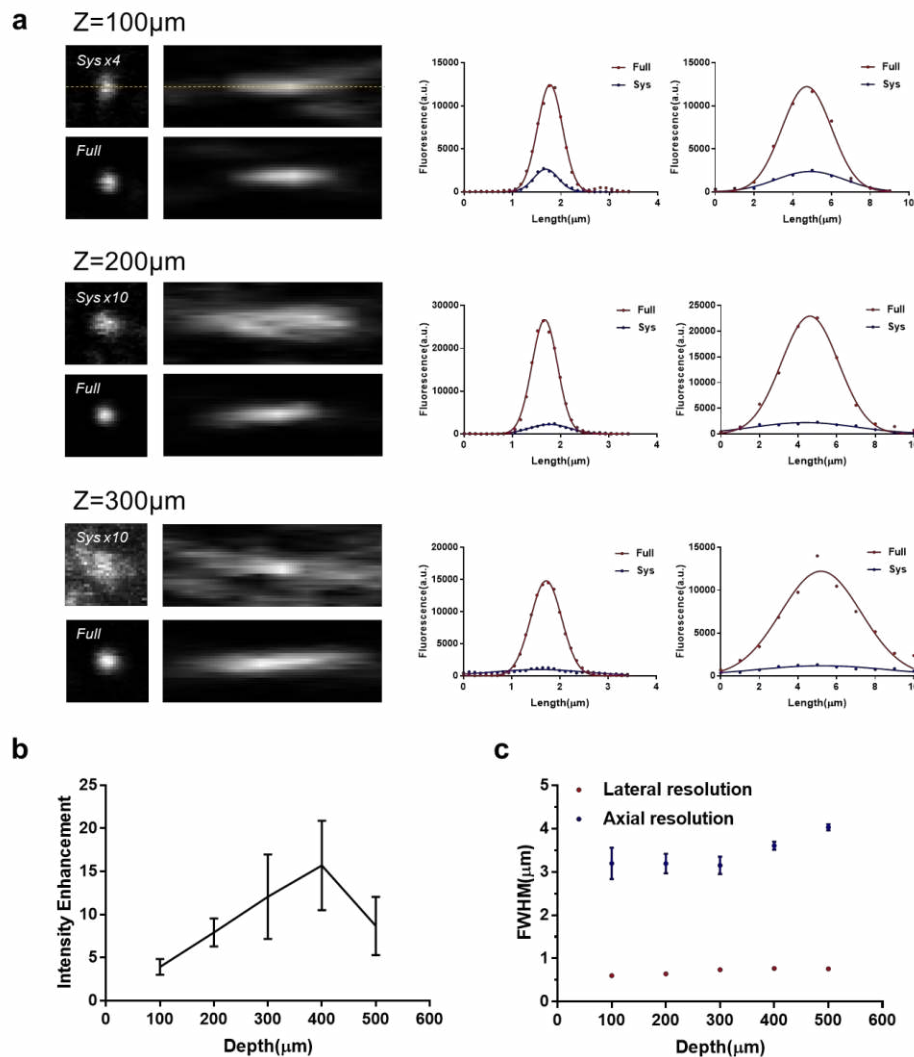**Fig. S12.** *In vitro* **characterization of aberrations of an optical clearing window.** (a) Left column: lateral and axial PSF measured with 200-nm-diameter fluorescent beads at different depths with system and full AO correction. The images with system correction were enhanced to visualize details. Middle column: lateral intensity profile along the dashed line with system (blue) and full (red) AO correction. Right column: axial intensity profile with system and full AO correction. Full AO correction was performed by averaging the guide star signal over $30 \times 30 \ \mu m^2$. (b) The improvement of fluorescence intensity by full AO correction at different depths. (c) The lateral (red) and axial (blue) resolution after full AO correction.
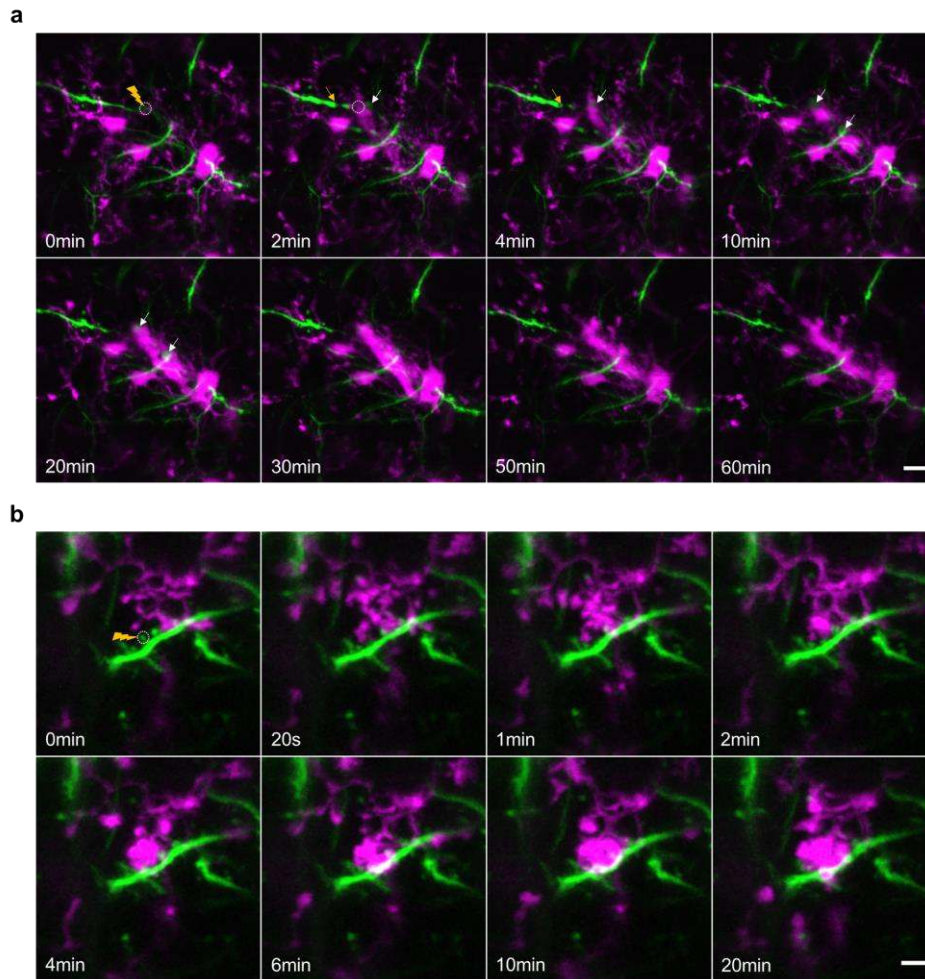
796
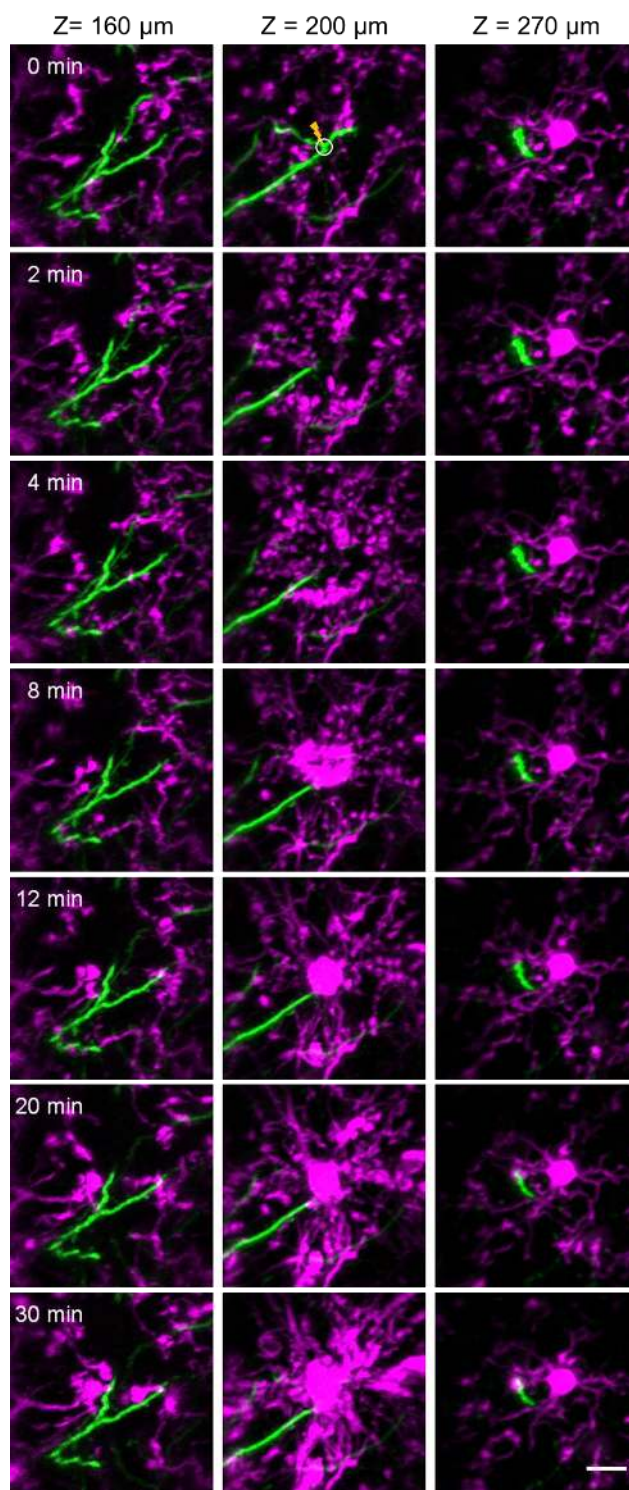
797
798
799 **Fig. S13 Time-lapse imaging of neurons (green) and microglia (magenta) in response to laser-**
800 **mediated lesion of the bifurcation of a primary apical dendrite.** The solid circle in the top panel
801 indicates the site of the laser injury. Scale bar: 10 µm.

802
803
804 **Fig. S14. AO enables *in vivo* study of neuron-microglia interaction after laser ablation of the**
805 **dendritic branch and a single spine**. (a) Time-lapse imaging of neuron (green) and microglia (magenta)
806 in response to laser dendrotomy on a tuft dendrite of the layer 5 pyramidal neuron. The injured region is
807 indicated by the dashed circle. Two white arrows indicate the retraction bulb formation at the proximal end
808 of the injured branch, and the yellow arrow indicates the dendritic segmentation at its distal end. The results
809 show that while the injured dendrite undergoes Wallerian-like degeneration at both distal and proximate
810 ends, the nearby microglial process only extended selectively to surround the proximate end of the
811 retraction bulb rather than the distal end. This phenomena may be potentially explained by different
812 signaling mechanisms for distal and proximate dendrites during neuronal degeneration. Scale bar: 10 µm.
813 (b) Time-lapse imaging of the dynamics of microglial processes in response to precise micro-lesion of a
814 single spine (dotted circle in the first frame) without damaging the dendritic shaft and nearby spines. In
815 contrast to laser cutting of the dendrite, this micro-lesion only triggers the activation of a few nearby
816 microglia, whose processes rapidly converged on the ablated spine as soon as 2 minutes after injury. Scale
817 bar: 5 µm.

818 **Table S1.** Wavefront sensing and imaging parameters.

Figure No.	Fluorescence labels	Imaging Depth (µm)	Excitation power (mW)	Average frames /slice	Pixel rate (pixels/s)	Voxel volume (µm³)	Guide star signal	Guide star Integration (s)
Fig. 1b Fig. S2	YFP	0~100	50	1	128K	0.39×0.39×2	N.A.	N.A.
		100~250	100	1				
		250~650	200	1				
Fig. 1f-g Fig. S7	YFP /Evans Blue	340~420	200	8	512K	0.2×0.2×2	Evans Blue	1
Fig. 2a-b	YFP /Evans Blue	0~125	50	8	512K	0.2×0.2×2	YFP	1~10
		125~225	100	8				
		225~475	200	8			Evans Blue	
		475~670	200	16				
Fig. 2d-e	GFP /Evans Blue	350~400	200	20	256K	0.23×0.23×2	Evans Blue	5
Fig. 3a	YFP	0~100	60	1	128K	0.6×0.6×2	N.A.	N.A.
		100~400	200	1				
Fig. 3b-c	YFP /Evans Blue	0~100	50	4	512K	0.2×0.2×2	YFP	1~20
		100~150	50	8	256K	0.4×0.4×2	Evans Blue	
		150~300	100	8				
		300~400	200	8				
		400~500	200	16				
		500~600	200	32				
Fig. 3d-e	GFP /Evans Blue	175~225	200	8	256K	0.23×0.23×2	Evans Blue	2
Fig. 4a-b	GFP /MeO-X04 /Evans Blue	220~280	200	16	256K	0.23×0.23×2	Evans Blue	1
Fig. 4c	YFP/GFP /Evans Blue	0~50	30	4	256K	0.4×0.4×2	YFP&GFP	1~5
		50~150	60	4				
		150~200	100	4				
		200~300	200	4			Evans Blue	
		300~400	200	8				
		400~450	200	16				
		450~600	200	24				
Fig. 4d-f Fig. S13	YFP/GFP /Evans Blue	140~180	100	2	256K	0.23×0.23×2	YFP&GFP	2
		180~220	100	4			Evans Blue	1
		250~290	200	8			Evans Blue	

38

819

Figure No.	Fluorescence labels	Imaging Depth (µm)	Excitation power (mW)	Average frames /slice	Pixel rate (pixels/s)	Voxel volume (µm³)	Guide star signal	Guide star Integration (s)
Fig. S5-6	Green beads /Evans Blue	0~175	30	1	256K	0.12×0.12×1	Evans Blue	1
		175~275	60	1				
		275~475	100	1				
		475~625	200	1				
Fig. S8	YFP /Evans Blue	0~100	30	4	512K	0.2×0.2×2	YFP	1
		100~300	60	8	256K	0.4×0.4×2	Evans Blue	1~20
		300~400	120	8				
		400~500	200	8				
		500~660	200	16				
Fig. S9	GFP	0~40	25	1	128K	0.5×0.5×2	N.A.	N.A.
Fig. S10b	GFP	0~100	60	1	128K	0.4×0.4×2	N.A.	N.A.
		100~200	200	1				
Fig. S11	GFP	0~40	80	1	128K	0.5×0.5×2	N.A.	N.A.
Fig. S12	Green beads /Evans Blue	0~75	30	1	256K	0.12×0.12×1	Evans Blue	1
		75~175	60	1				
		175~375	100	1				
		375~525	200	1				
Fig. S14a	YFP/GFP	110~150	100	1	128K	0.23×0.23×2	YFP&GFP	2
Fig. S14b	YFP/GFP	80~110	80	1	128K	0.23×0.23×2	YFP&GFP	1

820

821   **Movie S1 (separate file).** Time-lapse imaging of neuron-microglial interactions following precise laser
822   micro-lesion of bifurcation point of the primary apical dendrite of a layer 5 pyramidal neuron.
823
824   **Movie S2 (separate file).** Time-lapse imaging of microglial response to high-precision laser ablation of a
825   single spine.